Chemical Engineering Science 320 (2026) 122666

Contents lists available at ScienceDirect

Chemical Engineering Science

journal homepage: www.elsevier.com/locate/ces

Catalytic baeyer-villiger oxidation over N-doped carbon with aliphatic aldehyde: Mechanism, kinetic modeling, life cycle assessment, and techno-economic analysis

Jiangnan Huang [a,b,1], Chaoxu Chai [b,1], Hongjuan Wang [b], Hao-Fan Wang [b], Shuang Li [c], Hao Yu [b], Yonghai Cao [b,*]

[a] College of Chemistry and Chemical Engineering, Zhongkai University of Agriculture and Engineering, Guangzhou, Guangdong 510550, China
[b] School of Chemistry and Chemical Engineering, Guangdong Provincial Key Lab of Green Chemical Product Technology, South China University of Technology, Guangzhou 510641, China
[c] School of Biology and Biological Engineering, South China University of Technology, Guangzhou 510006, China

ARTICLE INFO

Keywords:
Carbon nanotubes
Cyclohexanone
Propionaldehyde
ε-caprolactone
N doping

ABSTRACT

ε-Caprolactone (ε-CL) is a key organic chemical intermediate and monomer for polycaprolactone (PCL). Developing a safe and cost-effective process for its efficient synthesis remains challenging. Here, a Baeyer-Villiger oxidation of cyclohexanone (Cy=O) using propionaldehyde (PRA) as a co-oxidant and N-doped carbon loaded carbon nanotubes (NDC@CNTs) as catalysts was conducted with a feature of the radical free reaction. The process achieves 40.14 % Cy=O conversion, 93.41 % ε-CL selectivity, and 0.36 aldehyde efficiency (AE). Good values of TON, STY and E-factor for the NDC@CNTs-catalyzed system showed the good scalability potential. The structure–activity relationship investigation showed that as the nitrogen content in NDC@CNTs increased, reaction activity rose and then declined. The ratio of pyridinic N to graphitic N (N_{Py}/N_G) was the key factor affecting activity. Mechanistic research revealed that NDC@CNTs boost overall reaction activity by accelerating PRA oxidation to peroxypropionic acid, which was crucial for the reaction. Kinetic studies determined the reaction orders and rate constants for Cy=O oxidation and PRA self-oxidation, establishing a predictable kinetic model through semi-batch reactions. LCA analysis reveals that this reaction system exerts a comparatively low pressure on global environmental reference systems. Moreover, the entire reaction process was meticulously designed and simulated using Aspen Plus software with a 98.77 % likelihood of positive unit profit (622.22 ~ 2909.06 USD/t), highlighting the good economic value.

1. Introduction

Environmental pollution control involves wastewater treatment (Kusuma et al., 2024a; Kusuma et al., 2024c; Zou et al., 2016), waste gas management (Az-Zahra et al., 2024; Hajivand et al., 2024), as well as the substitution of petrochemical products (Arista et al., 2024; Corma et al., 2001; Kusuma et al., 2024b; Meng et al., 2017; Putra et al., 2024; Singh et al., 2022). The escalating global demand for biodegradable polymers has established polycaprolactone (PCL) as a key material in sustainable manufacturing, due to its remarkable biodegradability, biocompatibility, and diverse applications in biomedical and environmental fields (Woodruff and Hutmacher, 2010). ε-Caprolactone (ε-CL), the monomer at the core of PCL production, has traditionally been synthesized through the Baeyer-Villiger (BV) oxidation of cyclohexanone (Cy=O) using hazardous peracids (e.g., peracetic acid and H_2O_2, etc.) (Baeyer and Villiger, 1899; Corma et al., 2001), which faces the inherent risks of instability, high costs, and intricate purification steps. Recent advancements have put forward a more environmentally friendly alternative, i.e., the O_2/aldehyde system, where aromatic aldehydes, such as benzaldehyde and m-chloro-benzaldehyde, function as sacrificial agents to activate molecular oxygen for ketone oxidation (Brink et al., 2004; Nabae et al., 2013). Meanwhile, among the efficient catalysts, carbon catalysts, including carbon black, carbon nanotubes (CNTs) and graphite, have revolutionized the BV oxidation by enabling high-

* Corresponding author.
E-mail address: meyhcao@scut.edu.cn (Y. Cao).
[1] These authors contributed equally.

https://doi.org/10.1016/j.ces.2025.122666
Received 1 April 2025; Received in revised form 9 September 2025; Accepted 20 September 2025
Available online 21 September 2025
0009-2509/© 2025 Elsevier Ltd. All rights are reserved, including those for text and data mining, AI training, and similar technologies.

efficiency reactions under mild conditions (Cai et al., 2022; Cai et al., 2025; Chen et al., 2017; Estes et al., 2019; Nabae et al., 2013). In this process, the unique sp^2-hybridized structures of these carbon catalysts facilitate the radical stabilization via π-π conjugated interactions between the benzene rings of the carbon surface and aromatic aldehydes, which is crucial for efficient chain propagation. For instance, Nabae et al. reported that Ketjen Black showed unique catalytic activity, over 90 % of ε-CL yield at 50 °C in the presence of benzaldehyde (Nabae et al., 2013). After that, graphite and CNTs were found to be efficient catalysts for this process (Cai et al., 2022; Chen et al., 2017; Li et al., 2013). All these studies demonstrated that the π-π conjugated interactions between benzaldehyde and carbons play vital role in the reaction. Furthermore, two main elementary steps were considered in this BV reaction: the oxidation of Cy=O and the aldehyde auto-oxidation (side reaction) (Cai et al., 2022; Cai et al., 2025). The aldehyde auto-oxidation directly yielding acid products would consume the key intermediate radicals, which greatly influenced the activity for the production of ε-CL. Nevertheless, the production of corresponding acid from the aromatic aldehydes significantly reduces economic viability, for instance, the price of benzaldehyde (~1,970 USD/t) typically is much higher than that of benzoic acid (~985 USD/t).

Aliphatic aldehydes are a class of organic compounds, which are of significance in the fields of chemistry and biochemistry, which would be transformed into active radicals (Timokhin et al., 2000; Yang et al., 2019). Propionaldehyde (PRA), as a representative, stands out as a promising candidate for BV oxidation (Pamin et al., 2015). The oxidation of PRA yields propionic acid (PA), a widely used commodity chemical in food preservation, agriculture, and pharmaceuticals, with market prices (~845.1 USD/t) closely matching those of PRA (~704.2 USD/t). Conventional carbon materials exhibit limited compatibility with aliphatic aldehydes in this reaction, which lack aromatic π-systems for π-π interactions with carbon surfaces. Nevertheless, ketjen black and acetaldehyde (2 equiv was used) were used for the production of ε-CL, displaying a 47 % CL yield with 0.27 aldehyde efficiency (AE) (Nabae et al., 2013). These results demonstrated that the potential of the carbons to stabilize reactive intermediates, such as acylperoxy radicals, even in the absence of aromatic conjugation-a feature unexplored in BV oxidation. Nevertheless, the unsurprisingly low EA was obtained for this process, which necessitates innovative modifications to enhance interfacial interactions between nanocarbon and substrates. The incorporation of heterogeneous atoms such as N, S, and B into the carbon skeleton is widely accepted to alter the surface electronic structure of carbon frameworks, facilitating the electron transfer and activating the aliphatic hydrocarbon substrates, for instance, the oxidative dehydrogenation of propane, butane, etc. (Cao et al., 2022; Liu et al., 2019; Zhang et al., 2024), the acetylene hydrochlorination (Wei et al., 2025a; Wei et al., 2025b), and the electrochemical of aliphatic hydrocarbon substrates (Grammenos et al., 2025). In these processes, heteroatom doping would enhance the C–H bond activation and O_2 adsorption, thus promoting the overall activity (Liu et al., 2019; Zhang et al., 2024). Inspired by these results, we believed that the surface modifications with heteroatom doping would efficiently tune the catalytic activity in the presence of aliphatic aldehydes.

In this study, we propose a novel catalytic system that combines N-doped carbon nanotubes with short-chain aliphatic aldehydes (i.e., PRA) for ε-CL synthesis. This approach addresses two critical challenges: (1) replacing benzaldehyde with PRA to enhance the techno-economy value, and (2) leveraging the tailored electronic properties of NDC@CNTs to overcome the inherent limitations of aliphatic aldehydes in radical-mediated reactions. By integrating kinetic studies and density functional theory (DFT) calculations, this work elucidates the synergistic role of NDC@CNTs in stabilizing PRA-derived radicals and accelerating oxygen transfer, thereby establishing a sustainable pathway for high-yield ε-CL production. Full-process simulation calculations with purities of all separated materials and economic analysis of this strategy are carried out to reveal the rationality of the synthesis process.

2. Results and discussions

2.1. Catalytic performance

A variety of carbon materials were employed as catalysts for the oxidation of Cy=O to produce ε-CL, which was summarized in Table 1. Before the reaction, the diffusion effect was eliminated (**Fig. S1**). In the blank experiment, a Cy=O conversion of 11.86 % and an ε-CL selectivity of 93.87 % were obtained, along with a PRA conversion of 75.02 %. The AE at this point was 0.15. The values of TON, STY and E-factor were calculated to be 2.67, 0.64 g $L^{-1}h^{-1}$ and 4.33, respectively. The introduction of nanocarbon materials such as activated carbon, graphite, diamond, and carbon nanotubes (CNTs) moderately enhanced the catalytic reaction efficiency. Among them, activated carbon, graphite, and diamond showed less significant activity enhancements, whereas CNTs (Fig. 1a) and NDC@CNTs (Fig. 1b and **Fig. S2**) effectively boosted the reactivity of both Cy=O and PRA. Specifically, under CNT catalysis, the conversion of Cy=O and PRA reached 22.52 % and 98.76 %, respectively, with an AE of 0.23. In this process, the values of TON, STY and E-factor were calculated to be 2.67, 1.27 g $L^{-1}h^{-1}$ and 2.82, respectively. This activity was close to that of Sn-zeolite beta (2.73, 1.30 g $L^{-1}h^{-1}$, and 2.70, respectively), which was the state-of-the-art catalyst for the production of ε-CL. After loading the mesoporous carbon with N dopant on the surface of NDC@CNTs, the catalytic activity further increased to 40.14 % and 100 %, and the AE rose to 0.36. This conclusion aligns well with our previous findings in the Cy=O/benzaldehyde reaction system (Cai et al., 2022), both indicating that NDC@CNTs are exceptionally effective catalysts in the BV oxidation of Cy=O. Meanwhile, the values of TON, STY and E-factor for the NDC@CNTs-catalyzed system were 4.50, 2.14 g $L^{-1}h^{-1}$, and 1.80, respectively, indicating the good scalability potential. The gas chromatography-mass spectrometry (GC–MS) analysis of the liquid sample after reaction was conducted, revealing that Cy=O, ε-CL, PRA and PA were observed without apparent by-products in this reaction (**Fig. S3**). Moreover, high-performance liquid chromatography (HPLC) was also used to analyze the obtained mixture after reaction (**Fig. S4**), we could observed five main peaks in the liquid chromatogram, corresponding to the PA, PRA, ε-CL, DCE, and Cy=O, respectively. And no other apparent impurity was observed. The mixture was then separated in a way of rectification under vacuum to obtain the purified product ε-CL. The nuclear magnetic resonance (NMR, ^1H and ^{13}C) analysis of the obtained ε-CL was then conducted (**Fig. S5**). The ^1H and ^{13}C NMR results confirmed that the target product was ε-CL. Although the specific surface area (SSA) of NDC@CNTs is slightly lower than that of CNTs due to the surface deposition synthesis process (Fu et al., 2020), the nitrogen species on the NDC@CNTs surface play a crucial catalytic role in enhancing the activity. The mesoporous carbons deposited on the NDC@CNTs surface also provide additional active sites and facilitate oxygen activation (Cao et al., 2018), significantly enhancing the efficiency of this reaction. Furthermore, the NDC@CNTs-catalyzed system exhibited a better AE (0.36), fully demonstrating that nitrogen species effectively promote the interaction between Cy=O and reaction intermediates. Additionally, NDC@CNTs displayed the highest normalized activity (14.64 mmol/m^2/h and 2167.56 mmol/g/h), which is much higher than other carbon catalysts. This activity was comparable to the state-of-art carbon catalysts with aromatic aldehydes, according to the polished literatures (**Table S1**). When dividing this reaction into two main processes: the Cy=O oxidation process and the aldehyde auto-oxidation reaction. Here, the aldehyde auto-oxidation reaction mean that the aldehyde directly react with O_2 to produce acid without interacting with Cy=O. This process would influence the efficiency of Cy=O oxidation and the utilization efficiency of aldehyde (i.e., AE). It was found that the activation energies for these two processes catalyzed by CNTs were 57.5 kJ/mol and 132.7 kJ/mol, respectively (Fig. 1c). When NDC@CNTs were used as the catalyst, the activation energies for these two reactions decreased to 44.8 kJ/mol and 92.1 kJ/mol (Fig. 1d), respectively, sufficiently illustrating that N doping effectively lowers the

Table 1
Catalytic performance over various nanocarbon catalysts.[a].

Catalyst	SSA[b] (m^2 g^{-1})	R_s[c] (mmol $m^{-2}h^{-1}$)	R_m[d] (mmol $g^{-1}h^{-1}$)	TON[e]	STY[f] (g $L^{-1}h^{-1}$)	Cy=O Conv. (%)	ε-CL Sel. (%)	PRA Conv. (%)	AE [g]	E-factor[h]
Blank	–	–	–	–	0.64	11.86	93.87	75.02	0.15	4.33
AC	495.0	0.08	38.88	1.68	0.80	15.55	90.25	88.98	0.16	4.06
Graphite	8.3	4.47	37.10	1.58	0.75	14.84	88.69	92.45	0.14	4.64
Diamond	2.1	15.06	31.63	1.36	0.65	12.65	89.47	90.98	0.12	5.41
CNTs	172.5	0.33	225.20	2.67	1.27	22.52	98.76	98.43	0.23	2.82
NDC@CNTs[i]	148.1	14.64	2167.56	4.50	2.14	40.14	93.41	100	0.36	1.80
DC@CNTs[j]	150.2	0.30	208.5	2.11	1.01	18.96	92.88	95.36	0.20	3.25
NDC@CNTs[k]	148.1	–	–	–		~0	–	–	–	–
NDC@CNTs[l]	148.1	–	–	–		<1	–	<1	–	–
NDC@CNTs[m]	148.1	–	–	–	1.98	38.62	90.02	99.2	0.33	1.97
Sn-zeolite beta	575.6	0.58	50.59	2.73	1.30	25.22	90.25	94.98	0.24	2.70

[a] Conditions: 35 ℃, 4 h, 0.5 MPa O_2, 1000 rpm, 10 mmol Cy=O, 10 mmol PRA, 10 mg catalysts, 36 mL DCE. [b] The specific surface area. [c] Initial rate of Cy=O consumption per m^2 of catalyst surface area. [d] Initial rate of Cy=O consumption per gram of catalyst. [e] Turnover number = $n_{ε\text{-CL}}/(n_{catalyst} \times t)$. [f] Space time yield = $m_{product}/(V_{reactor} \times t)$. [g] Calculated by (produced molar amount of ε-CL)/(consumed molar amount of BEA). [h] E-facor = $m_{waste}/m_{product}$. [i] Content of N dopant was 1.41 at.% (**Fig. S2**). [j] Deposited carbon on CNTs without N element. [k] Without PRA. [l] 200 mg PBQ was added. [m] The tenth recycle (**Fig. S7**).

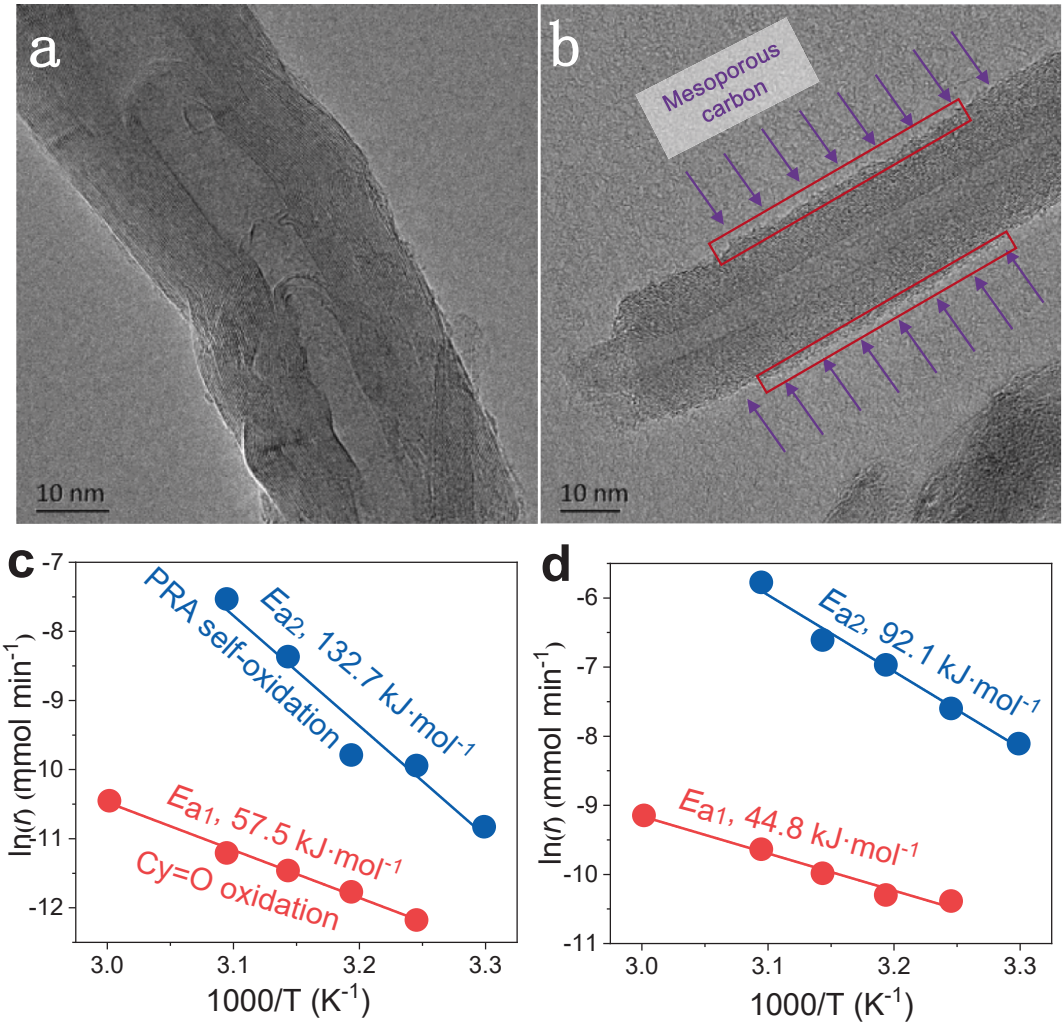

Fig. 1. TEM images of CNTs (a) and NDC@CNTs (b). The activation energy of tow elementary reactions catalyzed by CNTs (c) and NDC@CNTs (d).

energy barriers for both reactions. It was might argue that the comparably high SSA of NDC@CNTs was response for the enhanced activity. The DC@CNTs was prepared and displayed a lower activity for this reaction, confirming the enhancement of N dopants in this reaction. Moreover, the NH_3-TPD and CO_2-TPD to qualitatively analyze the acid-base properties of the catalysts were conducted. The results demonstrated that both the surface acid/base properties of NDC@CNTs were much higher than that of CNTs, which might be response for the high catalytic activity of NDC@CNTs for the production of ε-CL (Fig. S6).

It was noted that the there was no activity for this reaction without the aldehyde. Although N-doped carbons can activate the oxygen

molecule (Yang et al., 2017), the comparably low temperature was not conducive to activating oxygen molecules in this process. Generally, the activation of aldehyde with O_2 molecule is the initiate step for this reaction, deriving the acyl radicals, alkoxy radicals and acyl peroxyl radical, which promote the radical reaction and improve the overall activity (Nabae et al., 2013). Additionally, the introduction of the radical scavenger p-benzoquinone completely inhibited this reaction, indicating that it still followed a radical chain reaction mechanism (Su et al., 2017; Tang et al., 2016). The high stability of NDC@CNTs in this work was also observed, as the similar activity (38.62 % Cy=O conversion and 0.33 of AE) of the tenth-recycled NDC@CNTs was obtained (Table 1 and **Fig. S7**). The comprehensive characterizations were carried out (**Fig. S8**). TEM, XPS, Raman results demonstrated that no significantly change was observed between the pristine and the obtained carbon catalyst.

Numerous studies have demonstrated that solvents play a crucial role in liquid-phase reactions (Cao et al., 2017; Reichardt and Welton, 2011). Their inherent polarity, dielectric constant, and solvation effects can significantly alter the rate of chemical reactions, thereby influencing the final reaction activity. **Fig. S9** illustrate the impact of various solvents on the reaction activity of this system. The results indicated that the reaction performance was optimal when using DCE as the solvent, with a Cy=O conversion rate reaching 52.32 %. In contrast, the performance significantly declined when employing ethyl acetate, acetonitrile, and n-heptane as solvents. The worst performance was observed when toluene was used as the solvent, with a Cy=O conversion rate of only 9.17 % under the same conditions. This might be attributed to the strong interaction between toluene and carbon materials, which affected the role of the carbon surface on intermediate radicals and consequently reduced the reaction activity (Cao et al., 2017). Moreover, the high selectivity of PA could indirectly reflected that the presence of toluene promoted the auto-oxidation of PRA rather than enhancing the oxidation of Cy=O.

2.2. The effect of N doping

Nitrogen sites are generally recognized as important active sites on the surface of NDC@CNTs (Yu et al., 2011), and a detailed analysis of these sites could help us better understand the catalytic role of NDC@CNTs. In this study, we employed XPS to analyze the surface chemistry of different NDC@CNTs (**Fig. S2**). By extending the deposition time, it can be observed that the N content on the surface of NDC@CNTs gradually increased, which also demonstrated the effectiveness of the post-deposition method for preparing NDC@CNTs (Fu et al., 2020; Huang et al., 2022). The high-resolution N_{1s} spectra of XPS for five NDC@CNTs with different nitrogen contents were conducted (Fig. 2a) and the fitting parameters were summarized (**Table S2**). Five distinct N species were identified: pyridinic nitrogen (N_P) at 398.1 ± 0.1 eV, pyrrolic nitrogen (N_{Pyr}) at 399.5 ± 0.2 eV, graphitic nitrogen (N_G) at 401 ± 0.1 eV, nitrogen oxides (N_{OX}) at 403 ± 0.2 eV, and chemically adsorbed nitrogen (N_{Ads}) at 404.9 ± 0.3 eV (Cao et al., 2013). The results indicate that as the deposition time of pyridine increased in the precursor, the gross N content increased from 0.26 at.% to 4.51 at.%. During this process, the doping rate of nitrogen was not simply linearly related to the deposition time. A possible reason for this was that as N atoms continued to be doped into the carbon skeleton, the deposition of mesoporous carbons containing N species on NDC@CNTs became too thick, inhibiting subsequent deposition.

The catalytic performance of NDC@CNTs in the Cy=O oxidation in the presence of PRA was summarized (Table 2). When the content of N dopants varied, the conversion of Cy=O first increased and then declined. The highest conversion of Cy=O was 40.14 % with a 93.41 % selectivity of ε-CL when NDC@CNTs with 1.41 at.% N dopant was used. The decrease of activity catalyzed by NDC@CNTs with high N content (>1.41 at.%) could be explained that the high content of N dopant would facilitate the decomposition of peroxide intermediates derived from the PRA oxidation, which was significant for the Cy=O oxidation. To deeply investigate the role of N species in this reaction system, we correlated the content of gross N and N species with the formation rate of ε-CL (Fig. 2b). The relationship between the formation rate of ε-CL and the content of gross N resembled a volcano-shaped curve. When the content of gross N increased to 1.41 %, the formation rate of ε-CL reached the maximum, 93.74 mmol h^{-1} g^{-1}. This result could be ascribed to the modified surface electron density by N doping on NDC@CNTs, facilitating electron transfer between surface carbon and intermediates, thereby accelerating the reaction rate and promoting the formation of the product ε-CL (Cai et al., 2025). Subsequently, as the total nitrogen content continued to increase, the formation rate of ε-CL began to decline. When the content of gross N reached 4.51 %, the formation rate of ε-CL was 63.84 mmol h^{-1} g^{-1}. The decreased activity might be due to excessive N species inducing the decomposition of peroxides, which probably facilitate the aldehyde auto-oxidation yielding PA directly (Cai et al., 2022), thereby hindering the chain propagation of Cy=O oxidation process and ultimately slowing down

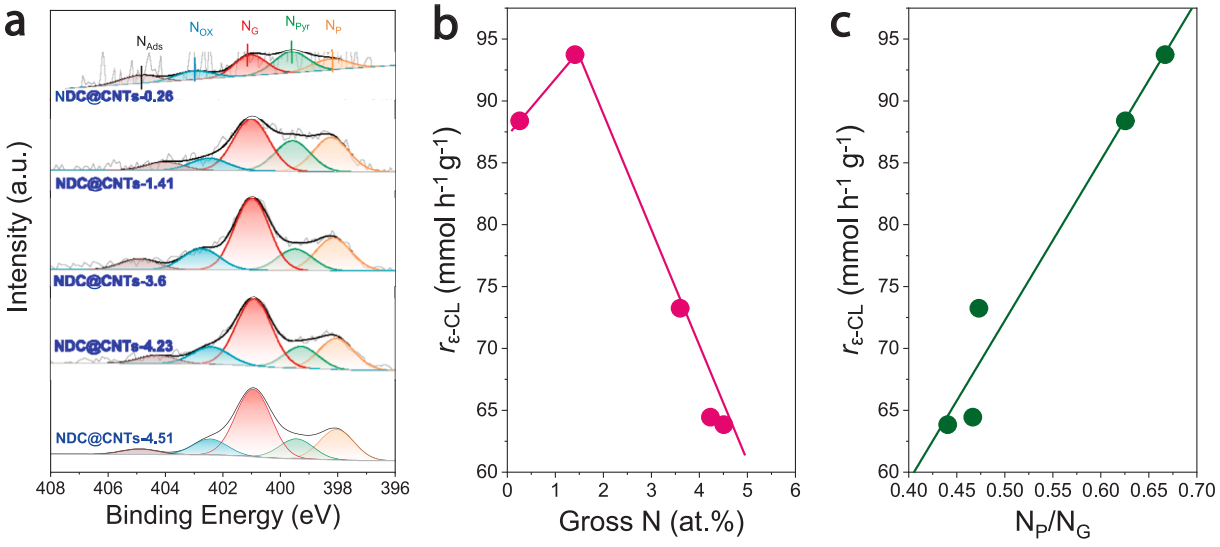

Fig. 2. (a) High resolution deconvolution of N_{1s} XPS spectra of NDC@CNTs catalysts. Dependence of the production rate of ε-CL on the gross N (b) and ratio of N1/N3 (c).

Table 2
The XPS analysis of N dopants on NDC@CNTs materials and their catalytic performance.[a].

Entry	N content (at. %)	N deconvolution (at. %)			N_P/N_G	TON[b]	STY[c] (g $L^{-1}h^{-1}$)	Basicity (mmol g^{-1})	Acidity (mmol g^{-1})	$r_{\varepsilon-CL}$(mmol $g^{-1}h^{-1}$)	Cy=O	ε-CL	AE [d]	E-factor[e]
		N_P	N_{Pyr}	N_G							Conv. (%)	Sel. (%)		
1	0.26	0.04	0.08	0.07	0.63	4.24	2.02	0.28	0.18	88.39	39.58	89.33	0.35	1.85
2	1.41	0.35	0.31	0.53	0.67	4.50	2.14	0.88	0.81	93.74	40.14	93.41	0.36	1.80
3	3.6	0.76	0.49	1.6	0.47	3.52	1.67	1.54	0.98	73.24	32.25	90.84	0.3	2.16
4	4.23	0.91	0.61	1.94	0.47	3.09	1.47	2.89	1.21	64.44	28.87	89.28	0.29	2.24
5	4.51	1.02	0.61	2.32	0.44	3.06	1.46	3.66	1.08	63.84	27.39	93.23	0.28	2.32

[a] Conditions: 35℃, 4 h, 0.5 MPa, 1000 rpm, 10 mmol Cy=O, 10 mmol PRA, 10 mg catalysts, 36 ml DCE. [b] Turnover number = $n_{\varepsilon\text{-CL}}/(n_{catalyst} \times t)$. [c] Space time yield = $m_{product}/(V_{reactor} \times t)$. [d] Calculated by (produced molar amount of ε-CL)/(consumed molar amount of BEA). [e]E-facor = $m_{waste}/m_{product}$.

the overall reaction rate. A similar tendency for the formation rate of ε-CL over N_p, N_{pyr}, and N_G was observed due to the significant influence of gross N (**Fig. S10**). Furthermore, the quantitative analysis of the surface basicity and acidity over N doped carbons were carried out (**Fig. S11**), in which the acidity sites and basicity sites on the carbon surface were tested by NH_3-TPD and CO_2-TPD, respectively In this process, we could observed that the surface basicity would greatly influence the activity, which is similar to that of the N dopants. Meanwhile, the chaotic relationship between surface acidity and activity was observed. These results demonstrated that the surface basicity was more important than the surface acidity to improve the catalytic activity.

For specific N species, the primary N species in NDC@CNTs are considered N_p and N_G. The previous work from our group has confirmed that the N_p and N_G might be responsible for the activity of Cy=O conversion in the presence of benzaldehyde (Cai et al., 2022). In this work, further analysis of the relationship between the N_P/N_G ratio and the formation rate of ε-CL revealed a linearly plotting (Fig. 2c), indicating that the distribution of N_P/N_G on the surface of NDC@CNTs was the key issue for modulate the catalytic activity for the production of ε-CL. Moreover, the N_P/N_G ratio would show a regulatory effect on surface electronic properties, thereby influencing catalytic activity. This is consistent with our previously observed phenomena (Cai et al., 2022).

The dependences of N content and N_P/N_G on TON, STY, and E-factor were revealed as well (**Fig. S12**). As the increase of N content, the value of TON and STY first increased and then decreased. Meanwhile, the value of E-factor first decreased and then increased. These results demonstrated that there was an optimal nitrogen content (1.41 at.%), which could enhance the potential for large-scale reaction. For the variation of N_P/N_G ratio, we could observed that the value of TON and STY increased accordingly, whereas the value of E-factor decreased, confirming that the potential for large-scale reaction of this system could be adjusted by increase the ratio of N_P/N_G.

2.3. The effect of oxygen functionality

Surface oxygen functional groups are often regarded as active sites or display a significant role in catalysis (Chi et al., 2016; Su et al., 2013). In the liquid-phase oxidation reactions, oxygen-containing groups on nanocarbon often exhibit negative catalytic effects by inhibiting the generation and transformation of the free radicals (Cao et al., 2014; Yu et al., 2011). This phenomenon is also observed in the preparation of ε-CL from Cy=O oxidation. Our previous work found that the presence of oxygen-containing groups on NDC@CNTs inhibited the self-oxidation process of aldehydes, thereby effectively increasing the AE but reducing the overall reaction activity (Cai et al., 2022). In this work, the influence of surface oxygen groups on the Cy=O oxidation in the presence of PRA was investigated. A series of o-CNTs with different content of surface oxygen groups were prepared via an HNO_3 treatment process (Table 3 and **Fig. S13**). It was observed that as the HNO_3 oxidation time increased, the content of surface oxygen-containing groups on o-CNTs gradually rose, from 0.62 at.% to 3.85 at.%. Catalytic results showed that the increase in oxygen content did not significantly reduce the activity, which was different from our previous work. These results might be ascribed to the weak interaction between the surface oxygen-containing groups and free radicals of aliphatic hydrocarbons. Subsequently, o-CNTs were annealed with a high-temperature treatment at 600 °C and 900 °C under an argon atmosphere to remove, in which process the content of the surface oxygen-containing functional groups decreased gradually to 1.45 at.% at 600 °C and 0.93 at.% at 900 °C. A significant improvement in the catalytic performance of these annealed o-CNTs was observed, especially, with a Cy=O conversion and AE of 44.76 % and 0.35 over o-CNTs annealed at 900 °C. Meanwhile, the control experiment of calcining non-oxidized CNTs at 900 °C was conducted. And we found that the activity of this treated CNTs displayed a slightly enhanced activity (35.86 % Cy=O conversion). This enhanced activity might be attributed to the exposed edge carbons, where the surface oxygen groups were removed. These exposed edge carbons could facilitate the activation of O_2 molecules to promote the free-radical process (Cao et al., 2018; Yang et al., 2013), thus improving the overall activity. Moreover, we have compared the O1s XPS analyses before and after oxidation to reveal the role of surface oxygen functionalities on the reaction (**Fig. S14**). Four peaks at 530.7 ± 0.2 eV, 531.7 ± 0.1 eV, 532.8 ± 0.1 eV and 533.6 ± 0.2 eV were attributed to quinonic C=O (O1), ketonic C=O (O2), etherlike C-O-C (O3) and hydroxyl C-OH (O4)

Table 3
The XPS analysis of oxygen functionality on CNTs materials and their catalytic performance.[a].

Treatment time (h)	Temperature (°C)	O (at.%)	TON[b]	STY[c] (g $L^{-1}h^{-1}$)	Cy=O Conv.(%)	ε-CL Sel.(%)	AE [d]	E-factor[e]
0	30	0.65	3.85	1.83	32.52	98.76	0.32	2.03
1	85	1.24	3.64	1.73	32.46	93.54	0.31	2.09
3	85	2.59	3.69	1.76	33.44	91.97	0.32	2.03
5	85	3.46	3.18	1.51	28.98	91.55	0.29	2.24
7	85	3.85	3.43	1.63	32.21	88.77	0.3	2.16
7	600	1.45	4.33	2.06	44.76	80.62	0.35	1.85
7	900	0.93	4.22	2.01	43.62	80.65	0.35	1.85
0[f]	900	0.35	4.09	1.94	35.86	94.96	0.32	2.03

[a] Conditions: 50 ℃, 4 h, 0.5 MPa O_2, 1000 rpm, 10 mmol Cy=O, 10 mmol PRA, 10 mg catalysts, 36 mL DCE. [b] Turnover number = $n_{\varepsilon\text{-CL}}/(n_{catalyst} \times t)$. [c] Space time yield = $m_{product}/(V_{reactor} \times t)$. [d] Calculated by (produced molar amount of ε-CL)/(consumed molar amount of BEA). [e]E-facor = $m_{waste}/m_{product}$. [f] Annealed at 900 °C directly.

groups, respectively. And we found that there was no significant change was observed on the O1s XPS analyses of the pristine CNTs and used one. Moreover, the chaotic relationships between the O content and TON, STY and E-factor were observed, indicating that the O content could not dominate the reaction for the large-scale application (**Fig. S15**).

2.4. Mechanism investigations

The mechanism investigation for the synthesis of ε-CL from Cy=O in the presence of PRA catalyzed by NDC@CNTs was carried out. Previous literature has extensively explored the reaction mechanism under the O_2/aldehyde oxidation system, and the widely accepted reaction pathway is mainly divided into two steps (**Eqs. I** and **II**) (Cai et al., 2025; Wang et al., 2024). The first one is the initiation of the free-radical chain, where the aldehyde undergoes an auto-oxidation process with O_2 to generate an acyl peroxide radical. The acyl peroxide radical then abstracts a hydrogen atom from another aldehyde molecule to form an acyl peroxide intermediate. The second one involves the oxidation of a ketone by the peroxide intermediate to produce equimolar amounts of an ester and an acid.

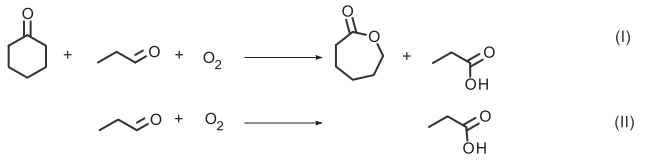

Notably, it is primarily the peroxide intermediate, rather than O_2 and aldehyde, that reacts directly with Cy=O in this process. According to the literatures, the peroxide intermediate is typically formed through the reaction between an aldehyde and O_2. However, the lifetime of this peroxide is a crucial parameter that affects its interaction with Cy=O. To verify the existence of the peroxide, Nabae et al. analyzed the intermediate products using infrared spectroscopy without adding ketones or solvents, ultimately detecting m-chloroperoxybenzoic acid in the products (Nabae et al., 2013). In this study, we employed an indirect approach to validate its presence. In this work, after 2 h of reaction and O_2 was stopped, Cy=O was added into the reaction system to verify whether the conversion of Cy=O would increase or not. As shown in Table 4, no apparent difference was observed between those experiments, suggesting that the self-oxidation of PRA indeed generated peroxypropionic acid intermediates, which reacted with Cy=O to form ε-CL. A deduction was that the reaction rate for peroxypropionic acid intermediates oxidizing Cy=O was much faster than the rate of intermediate decomposition, allowing for rapid consumption of the intermediates upon their generation. To verify the radical process and the role of N dopants in this reaction, the electron paramagnetic resonance (EPR) analysis of this oxidation catalyzed by CNTs and NDC@CNTs was conducted (**Fig. S16**). The results demonstrated that the low content of radicals was observed when CNTs was used as the catalysts. While, when NDC@CNTs was applied as the catalyst, abundant alkoxy and acyl peroxide radicals was obtained in the reaction (Stolze et al., 2002; Ueda et al., 1996). These results confirming that the reaction processes with CNTs and NDC@CNTs as the catalysts were the free-radical process, and the high performance of NDC@CNTs could be ascribed to its ability to efficiently promote the propagation of radicals in the reaction.

Table 4
Comparison of catalytic activity of NDC@CNTs under different reaction conditions.[a].

	Cy=O Conv. (%)	ε-CL Sel. (%)	PRA Conv. (%)	AE [b]
1	40.14	93.41	100	0.36
2[c]	38.82	98.52	100	0.38

[a] Conditions: 35 ℃, 4 h, 0.5 MPa O_2, 1000 rpm, 10 mmol Cy=O, 10 mmol PRA, 10 mg NDC@CNTs, 36 mL DCE; [b] Calculated by (produced molar amount of ε-CL)/(consumed molar amount of BEA). [c] Cy=O was added after 2 h without O_2, and continued the reaction for 2 h.

To further investigate the reaction pathway, we explored the effects of NDC@CNTs on PRA oxidation (Fig. 3). It was observed that a self-oxidation of PRA could be initiated even without a catalyst, with a remaining amount of 0.39 mol after 4 h of reaction. The addition of NDC@CNTs to the reaction system significantly enhanced the conversion of PRA, achieving 100 % conversion within 3 h. The presence of a significant amount of peroxypropionic acid intermediates during the reaction was observed in blank and NDC@CNTs-catalyzed systems, whose concentration initially increased with reaction time and then stabilized, a much higher amount than that of PA, indicating the incomplete decomposition of the intermediates to PA. To investigate whether the catalyst promoted the oxidation of Cy=O by peroxypropionic acid intermediates, we used peroxyacetic acid as the model peroxide, which was a aliphatic peroxide with the similar structure, due to the difficulty in obtaining peroxypropionic acid. The results showed that the addition of NDC@CNTs to this reaction system slightly improve the catalytic activity compared to the control experiment. Herein, we can conclude that NDC@CNTs enhanced the reactivity in the Cy=O/PRA oxidation reaction mainly by accelerating the first step of PRA oxidation. Meanwhile, the value of AE in the NDC@CNTs-catalyzed reaction was much higher than that of the one without N doping (Table 1), showing that N doping would enhance the interaction between peroxypropionic acid intermediates and Cy=O molecule.

N doping in nanocarbons is usually considered the key factor to enhance the catalytic activity of carbon catalyst (Fu et al., 2020; Tang et al., 2016; Yu et al., 2011). The interaction between carbon materials and substrates could be greatly enhanced with the incorporation with N dopant. Here, the uptakes of Cy=O and PRA in the presence of CNTs and NDC@CNTs were carried out (**Fig. S17**). The results demonstrated that the uptake capability of NDC@CNTs on both substrate (Cy=O and PRA) was much higher than that of CNTs. Furthermore, we used TPD and TGA-DSC analysis to reveal the difference between CNTs and NDC@CNTs to adsorb PR and Cy=O. The TPD results showed that NDC@CNTs displayed a much higher content of PR or Cy=O molecule adsorbed on the surface than those on CNTs, indicating that the PR and Cy=O molecule could be tightly interact with NDC@CNTs during the reaction (**Fig. S18**). Also, TGA results demonstrated that the lower residual quality over NDC@CNTs was observed than that over CNTs no matter Cy=O or PR, further confirming that the NDC@CNTs would be more favorable to adsorb the substrate to facilitate the reaction (**Fig. S19a and c**). The DSC analysis directly demonstrate the difference of adsorption enthalpies between carbons and substrates (**Fig. S19b and d**). When Cy=O was the substrate, tow peak centered at 143 °C and 275 °C, respectively, were observed. While, one peak was observed over CNTs (154 °C). This result indicated the higher adsorption enthalpies over NDC@CNTs, showing a stronger interaction between NDC@CNTs and Cy=O molecule. Similarly, when PR was the substrate, the peak centered at 183 °C over NDC@CNTs was higher than that over CNTs (160 °C), evidencing a stronger interaction between NDC@CNTs and PR molecule in this process. Overall, these results confirmed that N doping would greatly benefit the reaction via enhancing the interaction between carbons and substrates (Cy=O and PR).

The DFT simulations were further carried out, which would be helpful to understand the role of N dopants and the reaction mechanism (Fig. 4). In this study, pure graphene (G) and N-doped graphene (NG) were selected as the model carbon catalysts. According to the aforementioned discussions, the presence of carbon catalysts mainly influenced the activity of PRA and its derivate, which probably dominate the overall activity. Herein, PRA, propionyl (PRA*), peroxypropionyl (PRAOO*), and peroxypropionic acid (PRAOOH) were chosen as the substrates. The simulation results demonstrated that there were weak interactions between these substrates (PRA and its derivates) and G (−0.57 eV for $\Delta E_{a,\ PRA\text{-}G}$,-0.65 eV for $\Delta E_{a,\ PRA^*\text{-}G}$,-0.91 eV for $\Delta E_{a,\ PRAOO^*\text{-}}$

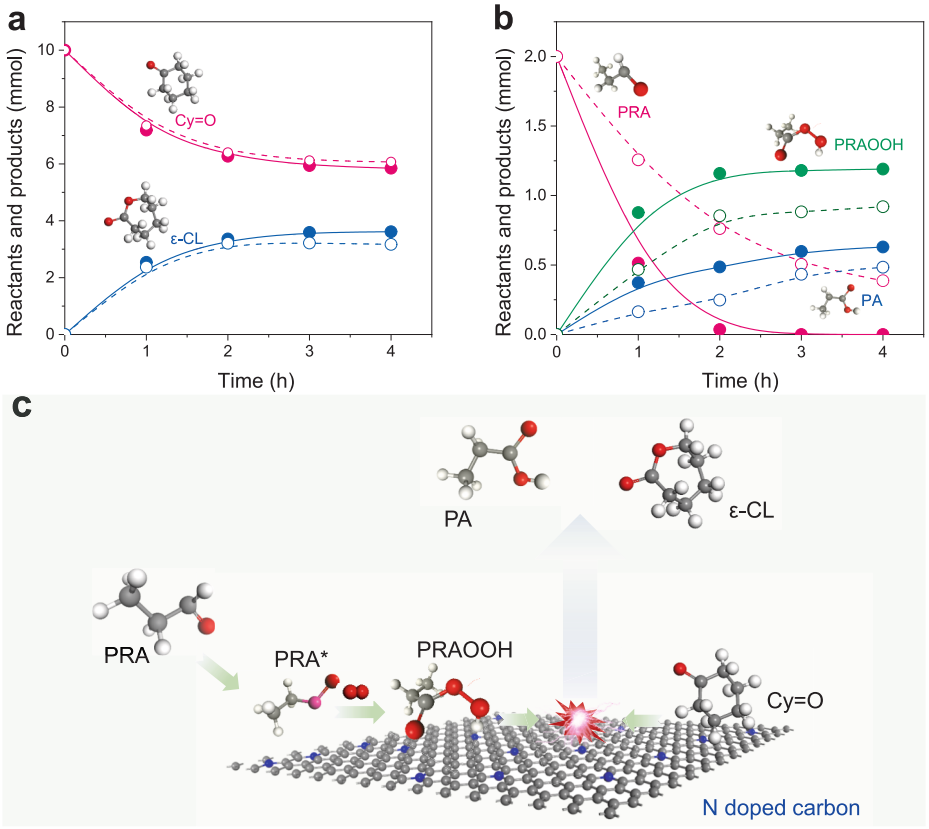

Fig. 3. The influence of the presence or absence of a catalyst on the oxidation of Cy=O by peroxy acids (a) and PRA oxidation (b). (c) Reaction mechanism of Cy=O oxidation in the presence of PRA catalyzed by NDC@CNTs.

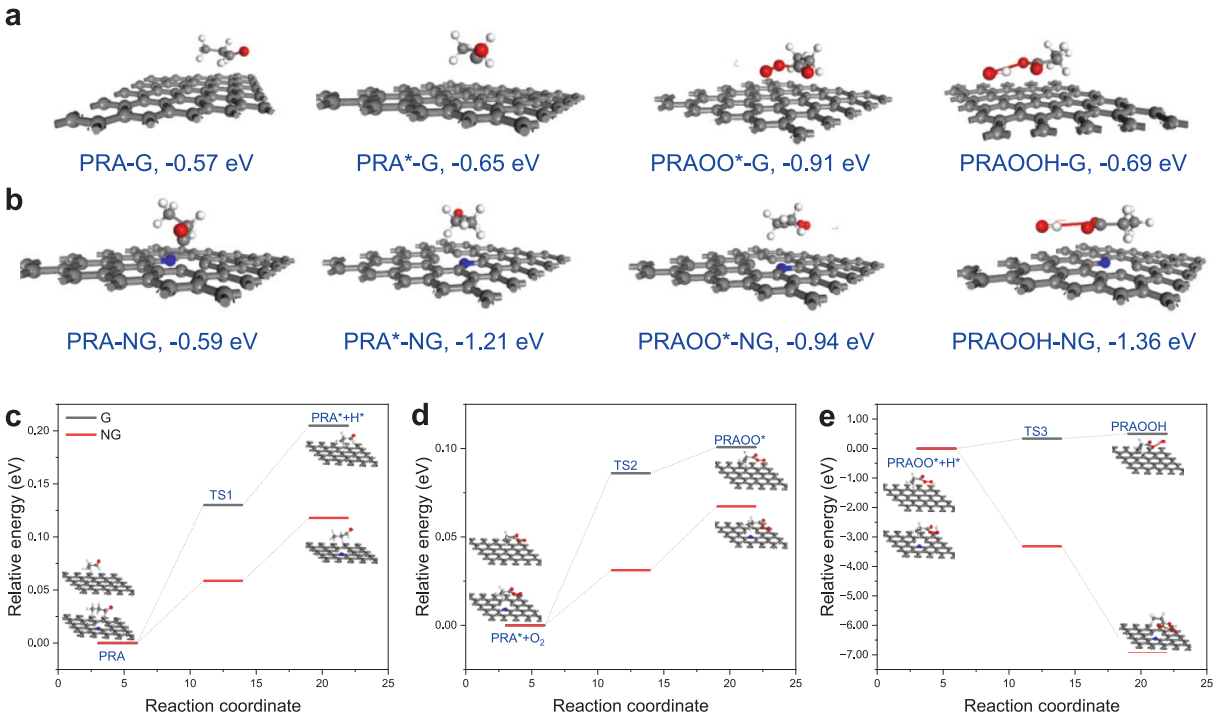

Fig. 4. Structural optimization and adsorption energy (a-b) and transition state simulation calculations (c-e) between the substrates and nanocarbon from the DFT calculation.

$_G$, and-0.69 eV for $\Delta E_{a,\ PRAOOH\text{-}G}$), ascribed to the short chain structure of PRA and its derivates. When NG was applied in this process, $\Delta E_{a,\ PRA\text{-}NG}$ and $\Delta E_{a,\ PRAOO^*\text{-}NG}$ were calculated as-0.59 eV and-0.94 eV, respectively, close to $\Delta E_{a,\ PRA\text{-}G}$ and $\Delta E_{a,\ PRAOO^*\text{-}G}$. Meanwhile, $\Delta E_{a,\ PRA^*\text{-}NG}$ and $\Delta E_{a,\ PRAOOH\text{-}NG}$ were calculated as-1.21 eV and-1.36 eV, respectively, much lower than $\Delta E_{a,\ PRA^*\text{-}G}$ and $\Delta E_{a,\ PRAOOH\text{-}G}$, indicating that the N dopant on carbon would enhance the surface adsorption of PRA* and PRAOOH. For a radical-free reaction, PRA* would react with O_2 to form PRAOO*, which would promote the radical-free chain reaction (Neuenschwander et al., 2010). The enhanced interaction between the N site and PRAOOH would benefit the decomposition of PRAOOH to produce more active radicals, thus facilitating the reaction. These results demonstrated that PRA and its derivate, i.e., acyl radical and peroxide radicals, could be adsorbed to carbon surface and react with adsorbed Cy=O to produce ε-CL (Fig. 3b), which well elaborate the experimental results.

Meanwhile, the oxidation process of PRA predominantly consisted of three critical stepwise reactions. Consequently, transition state simulation calculations were carried out for these reactions on the surfaces of both pure carbon materials and N-doped carbon materials. As illustrated in Fig. 4**c-e**, when N sites were present, the forward energy barrier for the elimination of a hydrogen radical from PRA (TS1) was notably low (0.06 eV), lower than the corresponding energy barrier for TS1 on pure carbon materials (0.13 eV). Regarding the formation of PRAOO* from PRA* and O_2 (TS2), the model incorporating nitrogen sites exhibited a forward energy barrier of 0.03 eV, in contrast to the 0.09 eV barrier observed for pure carbon materials. Furthermore, for the nitrogen-doped carbon catalyst containing nitrogen sites, the forward energy barrier for the reaction leading to the formation of PRAOOH from PRAOO* and H* (TS3) was −3.32 eV, substantially lower than the 0.34 eV barrier for pure carbon materials. By integrating the findings from adsorption simulations, it was evident that PRAOO* and H* could spontaneously combine and stably exist as PRAOOH at N sites. Therefore, in comparison to pure carbon materials, the presence of basic (nitrogen) sites not only aided in the stabilization of radicals generated on the carbon material surface but also accelerated the three pivotal radical reactions, ultimately boosting the overall reaction efficiency.

Furthermore, the calculation of energy levels for the highest occupied molecular orbital (HOMO) and the lowest unoccupied molecular orbital (LUMO) of materials, along with their energy difference ($\Delta E_{HOMO\text{-}LUMO}$) (Eq. 1), had become a cornerstone approach in catalytic materials science research for evaluating material stability and catalytic activity (Sharma et al., 2022; Zhao et al., 2024). Leveraging DFT theoretical calculations, we ascertained the $\Delta E_{HOMO\text{-}LUMO}$ values of carbon nanotubes containing varying nitrogen contents. Additionally, we delved into how the integration of nitrogen atoms within the carbon framework influenced the surface charge distribution of these nanotubes. **Fig. S20** displayed the correlation between the ratios of N_{Pyr} to N_G on the surface of carbon materials and their corresponding $\Delta E_{HOMO\text{-}LUMO}$ values. Remarkably, an escalation in the N_{Pyr} to N_G ratio corresponded to a reduction in the $\Delta E_{HOMO\text{-}LUMO}$ value of the model. This observation implied that the surface ratio of N_{Pyr} to N_G in carbon nanotubes could modulate the electron distribution on their surfaces. Specifically, a higher N_{Pyr} to N_G ratio facilitated electron transitions on the carbon surfaces, augmented electron transfer efficiency, and subsequently boosted the catalytic activity for PRA oxidation (Das et al., 2024). This outcome was in perfect harmony with the results gleaned from the experiments (Fig. 2c).

$$\Delta E_{HOMO-LUMO} = E_{LUMO} - E_{HOMO} \quad (1)$$

The operando DRIFTS analysis of the reaction catalyzed by carbon catalyst was performed (Fig. 5 **a-c**). The change of reaction temperature (30–80 °C) would greatly affect the generation of active radicals on the carbon surface, showing the dynamic surface state under reaction conditions. The results demonstrated that all the carbon materials, including CNTs, o-CNTs and NDC@CNTs, showed the efficient catalytic ability for this reaction. In this process, the intensities of peaks were enhanced alongside with the increase of reaction temperature from 35 °C to 65 °C. When the temperature was higher than 65 °C, the intensities of peaks decreased. These results demonstrated that the propagation of radicals would be accelerated (< 65 °C), which would be decomposed or annihilation quickly (>65 °C). It was observed that when o-CNTs was used as the catalyst, the typical radical reaction with

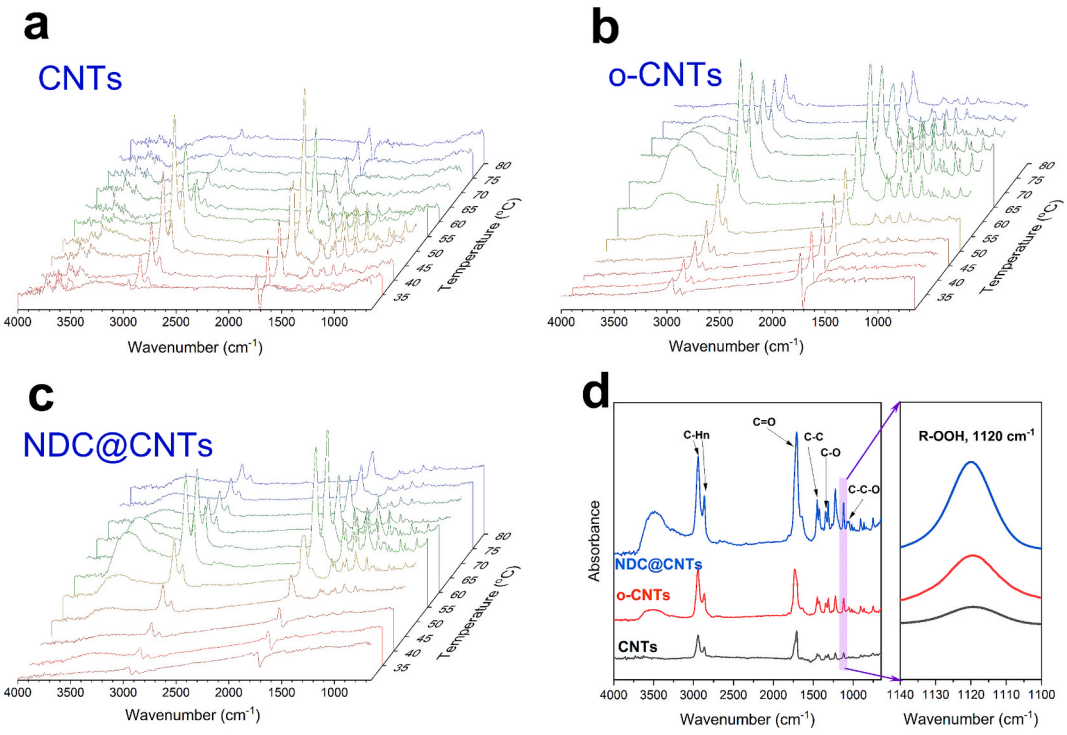

Fig. 5. The operando DRIFTS analysis of the mixture solution catalyzed by CNTs (a), o-CNTs (b), and NDC@CNTs (c) under different temperature. (d) Comparison of the FTIR spectra of solution catalyzed by nanocarbon catalysts at 55 °C.

enhanced activity was observed, similar to the CNTs-catalyzed system. The catalytic comparison of activity at 55 °C over NDC@CNTs, CNTs, and o-CNTs was then conducted (Fig. 5d). The main peak centered at 1120 cm^{-1} could be ascribed to the vibration of peroxide radical (R-OOH), which was the key intermediate for the reaction. It could be concluded that all these three carbon catalysts would facilitate the generation of R-OOH, and the strong intensity of the peak over NDC@CNTs was observed. This is the explanation for the reason why NDC@CNTs could display the highest activity in this reaction.

2.5. Kinetic modeling

An in-depth kinetic investigation of the reaction will help us uncover the essence of kinetic parameters and provide a solid theoretical foundation for potential future industrial-scale production, especially for the production of ε-CL (Wang et al., 2024; Yang et al., 2023). Also, the kinetic study to quantitatively analyze the role of NDC@CNTs and CNTs in this reaction would offer a deeper insight into the catalytic process. Previous research conducted by our research group has revealed that the aldehyde/O_2 reaction system for the production of ε-CL from Cy=O primarily consists of two core reactions (Cai et al., 2025): the oxidation of Cy=O and the auto-oxidation of PRA, as illustrated in **Eqs.** I and **II**, respectively.

Based on the aforementioned two main reactions, the primary reaction rate equation for Cy=O (A), PRA (B), and ε-CL (C), could be set. To obtain the reaction orders, several steps were carried out. When the initial concentration of Cy=O (C_{A0}) was equal to the initial concentration of PRA (C_{B0}), the kinetic equation can be simplified to **Eqs. 2–5**. By taking the logarithm of both sides of the equation, we can obtain a relationship diagram between the reaction rate (r_A) and the logarithm of C_A, and the slope q can be derived from this diagram through analysis. When C_{A0} is not equal to C_{B0}, we could obtain **Eqs. 6–7** through the reasonable mathematical derivation. Similarly, the slope of the straight line can be used to obtain *m*, and subsequently, n can be determined. Analogously, the reaction order for the self-oxidation of PRA can be solved as shown in **Eqs. 8–10**, and p can be obtained by plotting the relevant diagram.

$$-R_A = k_1 C_A^m C_B^n \tag{2}$$

$$q = m + n \tag{3}$$

When $C_A = C_B$,

$$-R_A = k_1 C_A^q \tag{4}$$

$$\mathrm{Log}(-R_A) = \mathrm{Log}k_1 + q\mathrm{Log}C_A \tag{5}$$

When

$$-R_A = k_1 C_A^m C_B^n = k_1 C_A^m C_B^{q-m} = k_1 C_B^q \left(\frac{C_A}{C_B}\right)^m \tag{6}$$

$$\mathrm{Log}\left(\frac{-R_A}{C_B^q}\right) = \mathrm{Log}k_1 + m\mathrm{Log}\frac{C_A}{C_B} \tag{7}$$

$$-R_B = k_1 C_A^m C_B^n + k_2 C_B^p \tag{8}$$

$$R_A - \frac{R_A}{\eta} = k_1 C_A^p \tag{9}$$

$$\mathrm{Log}\left(R_A - \frac{R_A}{\eta}\right) = \mathrm{Log}k_2 + p\mathrm{Log}C_B \tag{10}$$

The empirical data were collected and plotted (Fig. 6). The reaction orders (m, n, p) were calculated as 0.89, 0.99 and 1.87. Herein, the reaction rate constants k_1 and k_2 for those two main reactions could be obtained through parameter regression fitting of experimental data on the concentrations of various substances over time at different ketone-aldehyde molar ratios (4:1, 1:1, 1:2, and 1:3), using the Runge-Kutta method in MATLAB software (Fig. 7).(Su et al., 2023) It can be observed that there was a high degree of consistency between the experimental and fitted values. The calculated reaction rate constants k_1 and k_2 were 0.1103 L $mol^{-1}h^{-1}$ and 0.9524 L $mol^{-1}h^{-1}$, respectively, indicating that the self-oxidation of aldehydes would be faster than the BV oxidation in the presence of NDC@CNTs. Therefore, the reaction kinetic equations could be described as **Eqs.10–14**. To verify the reliability of the above model and parameter fitting data, a determinant coefficient test (ρ^2), an F-test (Fc), and a residual analysis (R^2) were conducted for calculation (**Eqs.15–17**). The obtained ρ^2 value was 0.995, meeting the requirement of the determinant coefficient test. The calculated Fc value was 215, which is greater than 10 times the $F_{0.05}$ (19). The R^2 value obtained from the residual analysis was 0.994 (Fig. S21). These results demonstrated the reliability of the established kinetic model and parameters.

$$-R_A = 0.11 C_A^{0.89} C_B^{0.99} \tag{10}$$

$$-R_B = 0.11 C_A^{0.89} C_B^{0.99} + 0.0.95 C_B^{1.87} \tag{12}$$

$$-R_C = 0.11 C_A^{0.89} C_B^{0.99} \tag{13}$$

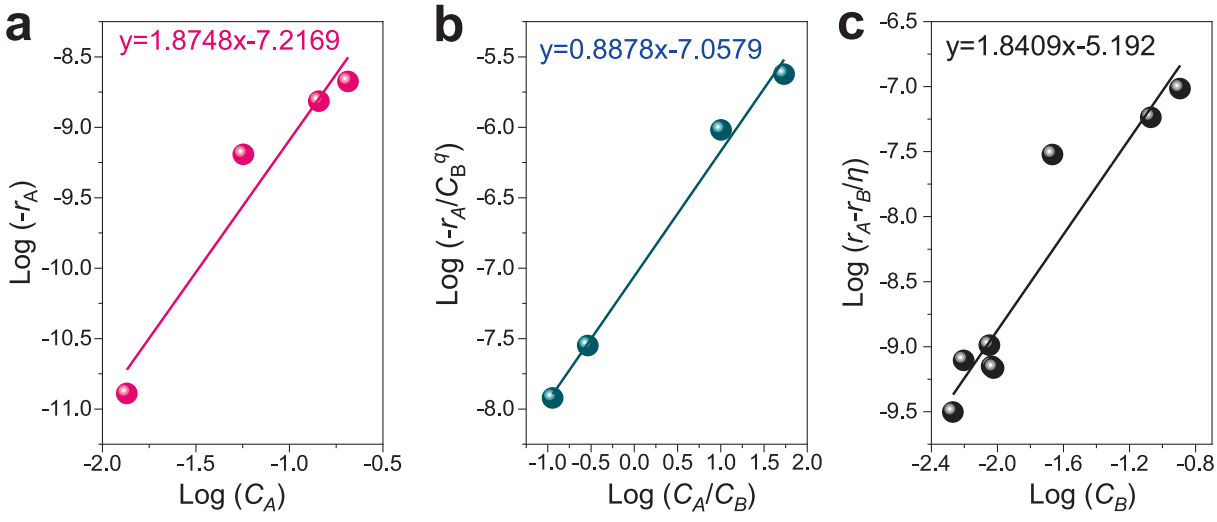

Fig. 6. Solutions of the reaction orders of (a) m, (b) q, (c) p.

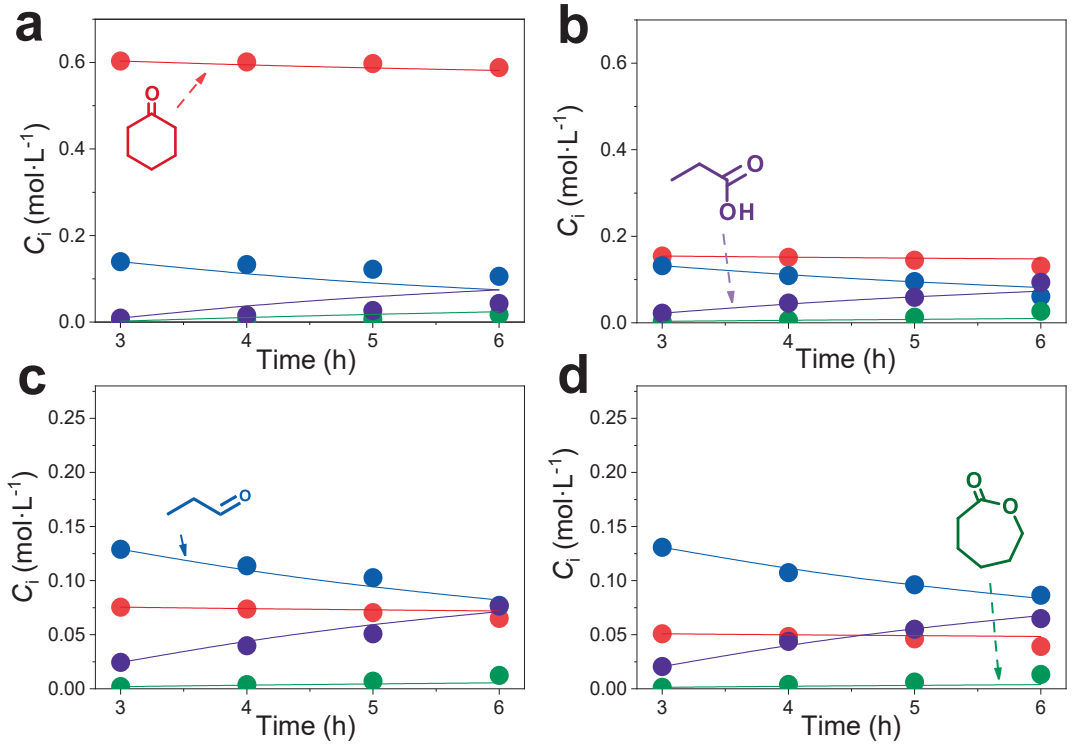

Fig. 7. Plots of empirical (dots) and simulated (curve) concentrations of substrates and products with RKA at (a) 4:1, (b) 1:1, (c) 1:2, and (d) 1:3.

$$-R_D = 0.11C_A^{0.89}C_B^{0.99} + 0.95C_B^{1.87} \tag{14}$$

$$\rho^2 = 1 - \frac{\sum_1^n (C_{e,i} - C_{c,i})^2}{\sum_1^n C_{e,i}^2} \tag{15}$$

$$F_c = \frac{[\sum_1^n (C_{e,i} - C_{c,i})^2]/P}{\sum_1^n (C_{e,i} - C_{c,i})^2/(n-P)} \tag{16}$$

$$R^2 = \frac{TSS - ESS}{TSS} = \frac{\sum_1^n (C_{e,i} - C_{ave,i})^2 - \sum_1^n (C_{e,i} - C_{c,i})^2}{\sum_1^n (C_{e,i} - C_{ave,i})^2} \tag{17}$$

where $C_{e,i}$ and $C_{c,i}$ represented the concentrations of each substance as determined by experiment and simulation, respectively. The variable n denoted the number of experimental data points, while P signified the number of fitting parameters. TSS (Total Sum of Squares) and ESS (Residual Sum of Squares) were statistical measures used in the analysis. Additionally, $C_{ave,i}$ refers to the average concentration of each substance obtained through experimentation.

Based on the aforementioned results, a prediction of the reaction could be performed. Combined with the obtained activation energy E_a (Fig. 1d) in the presence of NDC@CNTs, we can predict the catalytic performance of this reaction in the semi-batch reaction under different reaction conditions as well as the concentration trends of the reactants and products (Fig. 8). The concentration of each component was set according to **Eqs. 18–22**. Here, by comparing the simulated results with the experimental results, we find that the predictions were in high agreement with the experimental results, which fully validated the accuracy and reliability of the established kinetic model in this study.

$$-R_A = \frac{Q_B}{V_r}C_A + 0.11C_A^{0.89}C_B^{0.99} \tag{18}$$

$$-R_B = \frac{Q_B}{V_r}(C_{B0} - C_B) + 0.11C_A^{0.89}C_B^{0.99} + 0.0.95C_B^{1.87} \tag{19}$$

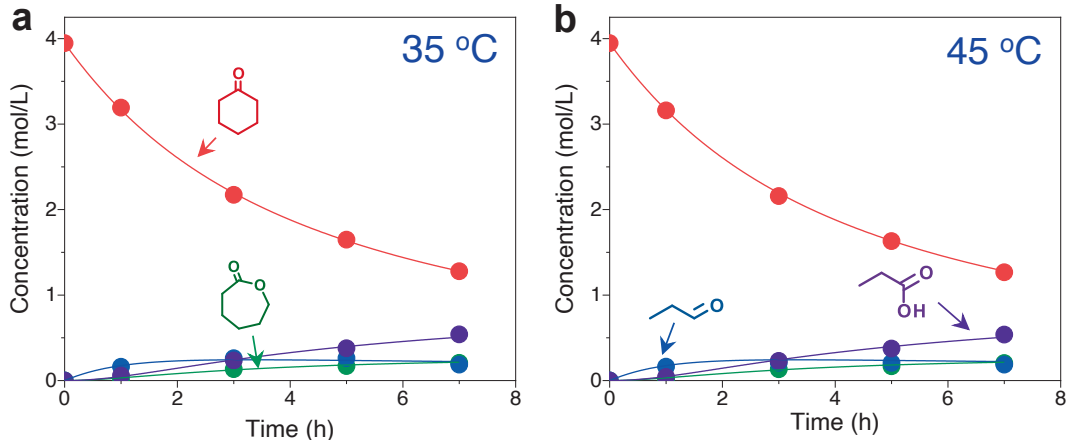

Fig. 8. The comparison of empirical data (dots) and simulation prediction (curve) of substrates and products distributions at 35 °C and 45 °C.

$$R_C = \frac{Q_B}{V_r}C_C + 0.11C_A^{0.89}C_B^{0.99} \quad (20)$$

$$R_D = \frac{Q_B}{V_r}C_D + 0.11C_A^{0.89}C_B^{0.99} + 0.95C_B^{1.87} \quad (21)$$

Where Q_B was the quantity of aldehyde flow, Vr was the volume of the reaction liquid. And the initial conditions were set as,

$$t = 0,\ C_A = C_B = C_C = C_D = 0,\ V_r = V_{r0} \quad (22)$$

Moreover, the comparison of the obtained kinetic parameters between PRA and benzaldehyde was conducted (Table S3). When benzaldehyde was used, k_1 and k_2 were 0.85 L $mol^{-1}h^{-1}$ and 0.08 h^{-1}, respectively, which was different from that of PRA. The high ratio of k_1/k_2 would benefit the production of ε-CL. That why the high AE was observed in the system with benzaldehyde. Meanwhile, the low activation energy was obtained with benzaldehyde (9.3 kJ/mol for Cy=O oxidation and 30.4 kJ/mol for Aldehyde auto-oxidation), showing that the reaction could be initiated more easily, which was also consistent with the experimental phenomena.

2.6. Full process simulations

The industrial-scale production of ε-CL is the final goal for a liquid-phase reaction. Here, we have designed a full-process simulation of the Cy=O/PRA reaction system using Aspen Plus V11 software for annually producing 1,000 tons of ε-CL in continuous operation mode, based on an annual production duration of 8,000 h (Fig. 9a). The reaction system primarily consisted of five components: Cy=O, PRA, ε-CL, PA, and O_2. The main property parameters of these components were listed in Table S4. To ensure more reasonable operating parameters, the

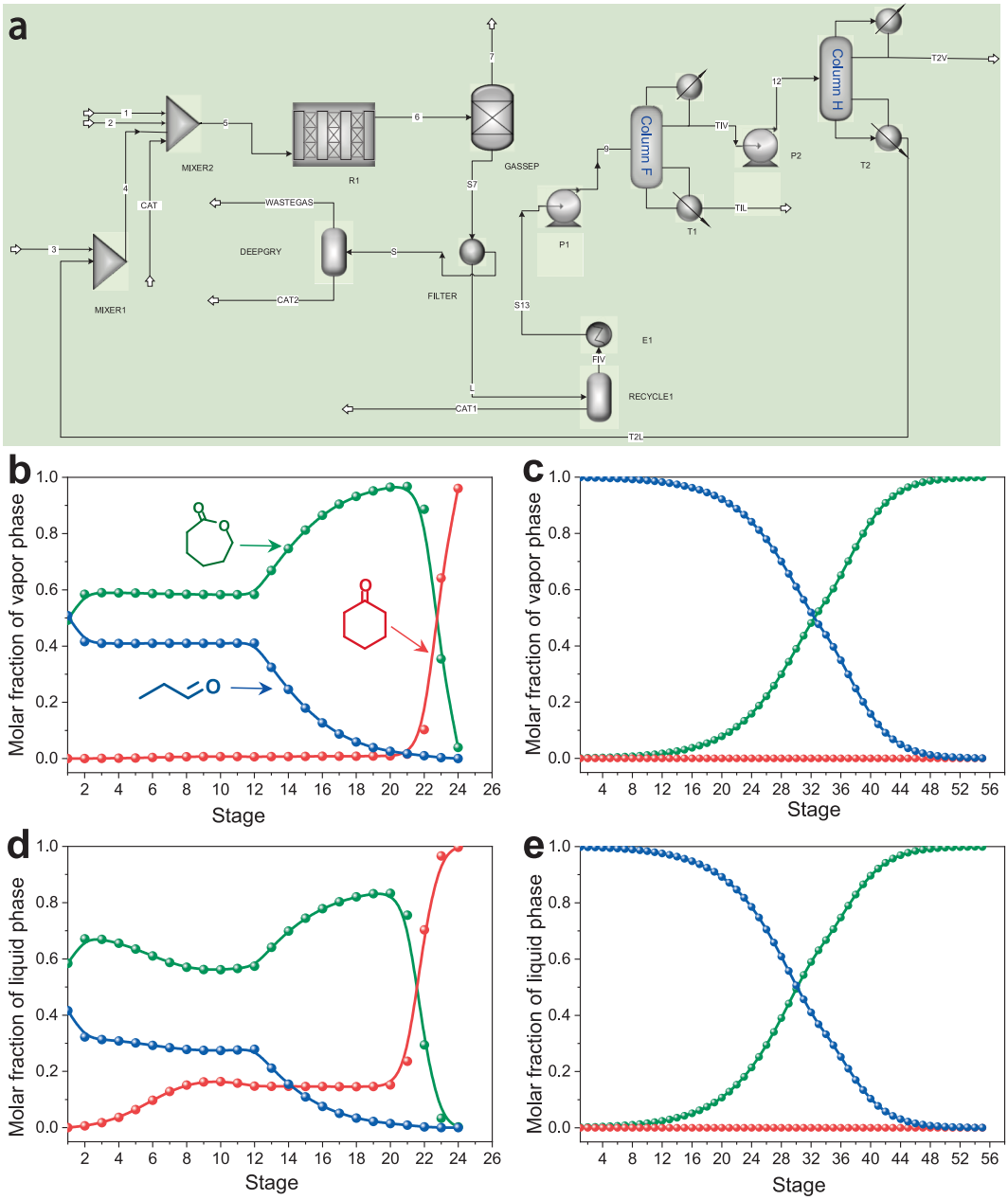

Fig. 9. (a) The process flow diagram of Cy=O/PRA oxidation reaction. Vapor-liquid phase composition distribution of each substance in the distillation column: (b) vapor phase composition distribution of tower F, (c) liquid phase composition distribution of tower F, (d) vapor phase composition distribution of tower H, (e) liquid phase composition distribution of tower H.

DSTWU module was first used for a simplified design of multicomponent distillation, yielding important parameters such as R_{min}, N_{min}, and N (**Table S5**). Subsequently, the RadFrac module was selected for rigorous calculations of the distillation column's separation capabilities and equipment parameters (Table 5). Considering that all substances were non-electrolytes and mostly polar (MUP > 0), the reaction system was a single liquid phase with intermolecular interactions, and ε-CL was prone to convert into dimers or high-molecular-weight polyesters upon heating process, the UNIQUAC-NRTL method for physical property simulation was herein selected.

The vapor–liquid phase composition distributions of each substance within the distillation columns were depicted in Figs. 9**b-c**. Distillation column F efficiently segregated the three materials into two distinct streams: the overhead stream comprised a blend of Cy=O and PA, whereas the bottom stream yielded high-purity ε-CL. It was noteworthy that the vapor–liquid phase composition underwent substantial changes on the 20th to 24th trays, which functioned as sensitive trays in the process. Figs. 9d and e revealed that distillation column H further refined the distillate from column F, producing pure PA at the overhead and pure Cy=O at the bottom. Consequently, with the specified operating parameters, the dual-column separation equipment successfully fulfilled the separation tasks for each substance (Table 5). At the outlet, following the process of fluid separation, the molar flow rates and molar fractions of each stream were precisely determined. Specifically, stream 11 from the bottom of distillation column F exhibited an ε-CL purity of 99.72 %. Stream 13 from the overhead of distillation column H boasted a PA purity of 99.86 %. Stream 14 from the bottom of distillation column H achieved a Cy=O purity of 99.89 %, with a circulating molar flow rate of 3.0759 kmol/h. These results unequivocally validated the effectiveness of the separation process and laied a solid foundation for future industrialization endeavors.

Moreover, industrial energy consumption was predominantly concentrated in auxiliary facilities such as water supply, electricity supply, and steam. According to **Table S6**, the feed plate numbers N_f for distillation columns F and H were set as 12 and 34, respectively, while the total theoretical plate numbers N were 24 and 55, respectively. With a plate spacing (H_T) of 0.4 m and a bottom space height (h) of 1 m, the height differences (Δz) between the feed pumps and the feed plates for columns F and H, were calculated using **Eq. 23**, were 5.8 m and 9.4 m, respectively. Since the pressure differences (ΔP) were 0, the lift heights (H) of the feed pumps for distillation columns F and H, derived from Bernoulli's equation (ignoring resistance loss terms, **Eq. 24**), were 5.8 m and 9.4 m, respectively. Further calculations directly yielded a shaft power (P) of 0.021 kW for booster pump G, while **Eq. 25** gave P of 0.0093 kW and 0.012 kW for the feed pumps of distillation columns F and H, respectively. Considering an annual production time (t) of 8000 h, the annual electricity consumption (W) could be calculated to be 170 kWh, 170 kWh, and 390 kWh (**Eqs. 26**), respectively.

$$\triangle z = H_T\,(N\text{-}N_f) + h \tag{23}$$

$$H = \Delta z + \frac{\Delta P}{\rho g} \tag{24}$$

$$P = Hqv\rho g \tag{25}$$

$$W = Pt \tag{26}$$

where $\triangle z$ was the height differences, H_T was the tray spacing, N was the number of actual plates, N_f was the feed plate number, h was the bottom space height, ΔP was the pressure differences, ρ was the density, g was the gravitational acceleration, P was the pressure, q was the flow rate, v was velocity, W was the annual electricity consumption, t was annual production time.

Herein, we could obtain that the heat load (Q_R) of the tubular reactor was 848,921 kJ/h, while the condenser heat loads (Q_C) for distillation columns F and H are 266,180 kJ/h and 741,953 kJ/h, respectively. Using tap water (T1 = 298.15 K) for cooling and setting the cooling water outlet temperature T2 to 333.15 K, with a constant-pressure specific heat capacity (C_p) of 4.2 kJ/kg·K in this temperature range, the annual cooling water consumptions mc of 46.16 kt, 103.09 kt, and 286.34 kt were yielded for the tubular reactor C and the condensers of distillation columns F and H, respectively (**Eq. 27**). Similarly, the product temperatures T3 for ε-CL and PA were 445.1 K and 386.5 K, respectively, with mass flow rates $q_{m,h}$ of 0.12 t/h and 0.16 t/h, and constant-pressure specific heat capacities (C_p) of 1.85 kJ/kg·K and 2.25 kJ/kg·K, respectively. Cooling the products to room temperature (T4 = 298.15 K) using tap water (T1 = 298.15 K) and setting the cooling water outlet temperature T2 to 333.15 K, the cooling water consumptions mc of 1.76 kt for both the ε-CL and PA product coolers were obtained subsequently (**Eq. 28**). Simulation results also showed that the reboiler heat loads for distillation columns F and H were 323,275 kJ/h and 792,640 kJ/h, respectively. Heating with saturated steam at atmospheric pressure (latent heat of vaporization (r) = 2258.4 kJ/kg) and discharging the condensate at saturation temperature, the heating steam consumptions m_h of 0.00038 kt and 1.63 kt were obtained for the reboilers of distillation columns F and H, respectively (**Eq. 29**).

$$m_c = \frac{Qt}{C_{Pc}(T_2 - T_1)} \tag{27}$$

$$m_c = \frac{q_{m,h}C_{Ph}t(T_3 - T_4)}{C_{Pc}(T_2 - T_1)} \tag{28}$$

$$m_h = \frac{Qt}{r} \tag{29}$$

Where m_c was the cooling water consumption, m_h was the heating steam consumption, Q was the thermal load, t was time, C_{Pc} was the specific heat at constant pressure, C_{Ph} was the heat capacity at constant pressure, T_1 was inlet temperature, T_2 was the outlet temperature, T_3 and T4 were the product temperatures, $q_{m,h}$ was the mass flow rate, r was the latent heat of vaporization.

2.7. Life Cycle assessment (LCA) analysis

LCA study with cradle-to-gate boundaries is the key issue for the process of manufacture, consumption and disposal of feed stock and energy (Sun et al., 2024). In this work, LCA methodology was used to analyze the environmental impact of our reaction process (**Fig. S22** and Table 6), from which several parameters were obtained. The results demonstrated that greenhouse-gas (GHG) emissions correspond to a global warming potential (GWP) of 0.08446 kg CO_2-eq, a comparatively high value that highlights a notable contribution to climate forcing. Fossil-resource depletion, expressed as the abiotic depletion potential for fossil resources (ADP(f)), amounts to 1.663 MJ; its normalized score is extremely small, indicating a minor share in the overall global

Table 5
Main parameters and the separation calculated results with the RadFrac module.

Compounds	Temperature (℃)	Pressure (bar)	Molar flow (kmol·h^{-1})	Molar flow (kmol·h^{-1})			Molar fraction		
				TIL	T2V	T2L	TIL	T2V	T2L
Cy=O	25	1	10	0.0031	0.0031	3.0759	0.0028	0.0014	0.9989
ε-CL	25	1	2.19	1.0888	0	0.0011	0.9972	0	0.0004
PA	25	1	1.095	0	2.19	0.0022	0	0.9986	0.0007

Table 6
LCA parameter values of this reaction system.

Impact categories	Value[a] GHG emission (kg CO_2 eq.)	ADP(f) (MJ)	HTP (kg DCB eq.)	TETP (kg DCB eq.)	POCP (kg C_2H_4 eq.)	ODP (kg R11 eq.)	AP (kg SO_2 eq.)	EP (kg Phosphate eq.)	FAETP (kg DCB eq.)	MAETP (kg DCB eq.)
Characteristic total value	8.446×10^{-2}	1.663	1.015×10^{-3}	4.337×10^{-4}	3.217×10^{-5}	1.527×10^{-14}	4.145×10^{-4}	2.119×10^{-5}	2.482×10^{-4}	4.723
Normalized value	1.861×10^{-14}	2.373×10^{-13}	2.794×10^{-15}	2.706×10^{-15}	5.682×10^{-15}	4.171×10^{-22}	3.063×10^{-14}	1.058×10^{-14}	8.853×10^{-16}	1.647×10^{-13}

[a] GHG: Global Greenhouse Gas. ADP(f): Abiotic depletion potential. HTP: Human toxicity potential. TETP: Terrestric ecotoxicity potential. POCP: Photochem ozone creation potential. ODP: Ozone layer depletion potential. AP: Acidification potential. EP: Eutrophication potential. FAETP: Freshwater aquatic ecotoxicity. MAETP: Marine aquatic ecotoxicity. DCB: 1,4-Dichlorobenzene. R11: Trichlorofluoromethane. Based on different environmental impact indicators, the contribution of different substances to the same environmental impact has been translated into harmonized baseline units.

resource burden. Human toxicity potential (HTP) is 0.001015 kg 1,4-dichlorobenzene-equivalent (DCB-eq), denoting a limited incremental health risk. Terrestrial ecotoxicity potential (TETP) reaches 0.0004337 kg DCB-eq, implying a non-significant potential impact on soil biota. Photochemical ozone-creation potential (POCP) is 0.00003217 kg ethene-eq, a marginal level with negligible smog formation. Ozone-depletion potential (ODP) is practically zero and can therefore be disregarded. Acidification potential (AP) is 0.0004145 kg SO_2-eq, suggesting negligible acid stress on soils and aquatic systems. Eutrophication potential (EP) is 0.00002119 kg PO_4^{3-}-eq, below the threshold of concern for algal proliferation. Fresh-water ecotoxicity potential (FAETP) is 0.0002482 kg DCB-eq, resulting in only slight toxic pressure on aquatic organisms. In stark contrast, marine ecotoxicity potential (MAETP) is 4.723 kg DCB-eq—the dominant environmental burden of the process. Meanwhile, following the normalization, all impact scores become extremely small (ranging from 10^{-13} to 10^{-22}), confirming that the process exerts a comparatively low pressure on global environmental reference systems. Nevertheless, MAETP and GWP warrant continued attention.

At the characterization level, MAETP and GWP emerge as the two pivotal impact categories, exhibiting the highest absolute scores. A contribution analysis reveals that for GWP, the steam-conversion process is the primary driver, accounting for 0.07666 kg CO_2-eq (90.8 % of the total), whereas Cy=O adds 0.006484 kg CO_2-eq (7.7 %). All remaining flows, including DCE solvent at 0.0003963 kg CO_2-eq, are minor. Analogously, MAETP is overwhelmingly dominated by the steam-conversion process, contributing 4.410 kg DCB-eq (93.4 %), with Cy=O contributing 0.2225 kg DCB-eq (4.7 %). Meanwhile, all other contributions are negligible. Overall, the results demonstrate that steam conversion—likely linked to energy generation—and Cy=O feedstock are the dominant impact sources, reflecting the process's high thermal demand (e.g., heating and separation). Consequently, future research should prioritize the mitigation of steam-related impacts, for instance through the adoption of renewable energy or highly efficient steam systems, to achieve substantial reductions in both GWP and MAETP. Concurrent optimization of Cy=O use, or the substitution of Cy=O with a less toxic alternative, could further attenuate ecotoxicity burdens.

2.8. Techno-economic and sensitivity analysis

To gain a deeper understanding of the economic feasibility of the Cy=O/PRA oxidation reaction system, we conducted a straightforward assessment of its costs and profits. A summary of all the simulated energy consumptions, cost of raw materials, and income from the products were summarized (Table 7 **and S7)**. For each ton of ε-CL produced, the electricity consumption, water consumption, and steam consumption were 0.73 kWh, 439.11 t, and 5.95 t, respectively. Additionally, when only considering raw materials and products while disregarding other costs associated with the production process, the total costs for producing 1 tonne of ε-CL amounted to 3101.09 USD. The total revenue generated from this production was 6181.82 USD per tonne of ε-CL, resulting in a profit of 3080.73 USD per tonne of ε-CL. Consequently, this process enabled the efficient production of ε-CL with considerable economic benefits. It is noteworthy that, compared to the amount of substrate used, the quantity of catalyst required was negligible (ppm level).

Economic sensitivity is closely linked to a product's ability to adapt to market fluctuations and serves as a validation of the process's feasibility. This study offers a comprehensive examination of how variations in the prices of raw materials and desired products influence the ultimate returns (Fig. 10). Here, the Monte Carlo simulation approach for uncertainty analysis was conducted. According to the market price variations of key components over the past year, it was postulated that each price variable adhered to a triangular distribution, where the median denoted the most likely value, and the minimum and maximum values aligned with the lower and upper limits of their historical fluctuation spans, respectively. The distribution parameters for each variable were detailed in **Table S8**. Using NumPy's np.random.triangular function, sample data for each key component were generated, with a total of 10,000 samples per variable. Subsequently, the profit corresponding to each sample was computed, and statistical analysis was

Table 7
Techno-economic analysis of the Cy=O/PRA oxidation reaction system.

		Molar mass ($g \cdot mol^{-1}$)	Input (ton)	Consume (ton)	UnitConsumption ($t \cdot t^{-1}$) or ($kWh \cdot t^{-1}$)	Unit price (USD)	Sub (USD)
Input	Cy=O	98.14	0.94	0.53	1.06	1101.93	1168.04
	PRA	58.08	0.56	0.56	1.12	1239.67	1388.43
	O_2	32	0.32	0.32	0.64	137.74	130.85
	NDC@CNTs	12	3×10^{-5}	3×10^{-5}	6×10^{-5}	~14000	~0.84
	Electricity	–	–	–	0.73	0.08	0.058
	Water	–	–	–	439.11	0.47	206.38
	Steam	–	–	–	5.95	27.55	163.92
	In total	–	–	–	–		3101.09
Output	ε-CL	114.14	–	0.50	1.00	4958.68	4958.68
	PA	74.08	–	0.55	1.11	1101.93	1223.14
	In total	–	–	–	–	–	6181.82
Profit	–	–	–	–	–	–	3080.73

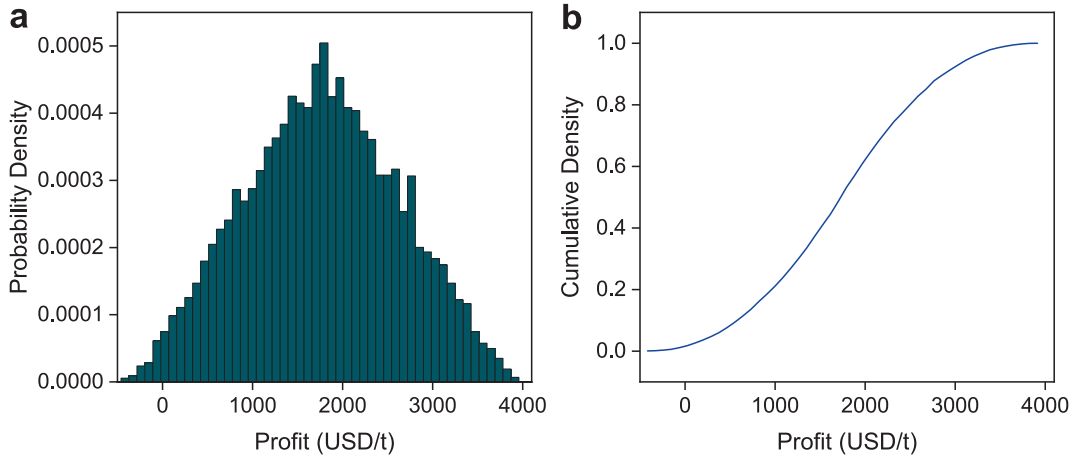

Fig. 10. Monte Carlo analysis of the profits sensitivity.

conducted on the resultant profit distribution, encompassing metrics like the mean, median, confidence interval, and the probabilities of profitability and loss (Table S9). Additionally, the profit distribution was visualized through Seaborn and Matplotlib, incorporating probability density histograms and cumulative probability curves.

An examination of the Monte Carlo simulation outcomes revealed that the mean profit per unit product stood at 1773.20 USD/t, while the median was 1780.33 USD/t. The narrow disparity between these two figures hinted at an approximately symmetric profit distribution. The marginally higher median relative to the mean suggested a potential slight rightward skew in the distribution, with profit values predominantly clustering above the average. The minimum profit registered at −435.99 USD/t, indicating a tangible risk of loss for the project under extreme market conditions, such as a substantial surge in raw material prices or a marked decline in product prices. Conversely, the maximum profit soared to 3961.71 USD/t, highlighting the considerable potential for profit growth under favorable market circumstances. From a quantile standpoint, the 10th percentile (P10) was 622.22 USD/t, implying that in 90 % of the simulated scenarios, the unit profit surpassed this threshold, further underscoring the project's resilience. A thorough analysis of various quantiles revealed that profits were predominantly concentrated within the 622.22 to 2909.06 USD/t range, suggesting that the project could attain relatively high economic returns under most conditions. In terms of risk evaluation, the simulation results indicated a 98.77 % likelihood of positive unit profit and a mere 1.23 % probability of loss. This finding signified that, under the current parameter assumptions and price fluctuation model, the project demonstrated robust economic feasibility and resilience against risks.

2.9. Bibliometric analysis

Moreover, the bibliometric analysis of the field of ε-CL production from the aldehyde/O_2 system during the past decades would offer the global research dynamics and tendency (Kusuma et al., 2024a; Kusuma et al., 2024c; Putra et al., 2024). Based on the Socoup database with "ε-CL" and "aldehyde" as the keywords in the 1996 to 2025 interval, 119 documents were obtained. The production of ε-CL from the aldehyde/O_2 system is a field with the constant attention (Fig. S23). Based on the bibliometric analysis generated by VOSviewer including keyword co-occurrence mapping, co-citation networks, publication trend analysis, and so on, a visual representation of the intricate connections and relationships within the scholarly landscape of relative issues were obtained. From the co-occurrence of keywords, the investigation of the reaction process for the production of ε-CL is most important (Fig. S24). The utilization of ε-CL for the production of polycaprolactone or other applications is also involved. The co-citation of authors analysis reveals that the presence of 47,906 links underscores the extensive collaborative connections and share citations among authors in the field (Fig. S25). The bibliographic coupling of countries analysis highlights China, United States, Germany, and India as the key contributors to the production and application of ε-CL in the field (Fig. S26).

3. Conclusions

In conclusion, the preparation of ε-CL from the oxidation of Cy=O in the presence of PRA catalyzed by NDC@CNTs was developed. N doping would facilitate the reaction process and recyclability, displaying the considerable conversion of Cy=O (40.14 %) and PRA (93.41 %) with an AE of 0.36. Meanwhile, the values of TON, STY and E-factor for the NDC@CNTs-catalyzed system were 4.50, 2.14 g $L^{-1}h^{-1}$, and 1.80, respectively, showing the good scalability potential. The ratio of N_p and N_G exhibited a synergistic effect on the promotion of activity. The introduction of oxygen-containing functional groups had no significant impact, while the edges carbons might be favorable for the improvement of the production of ε-CL. Mechanistic studies revealed that N dopants benefited the radical propagation of the reaction, and the key steps for the transformation of various radicals. The carbon catalyst enhanced the reaction activity by accelerating the first step of PRA oxidation to peroxypropionic acid, which would react with Cy=O yielding ε-CL. The kinetic study demonstrated that the reaction rate constants and activation energy over NDC@CNTs for the BV oxidation yielding ε-CL were 0.1103 $L{\cdot}mol^{-1}h^{-1}$ and 44.8 $kJ{\cdot}mol^{-1}$, lower than that of the self-oxidation of aldehyde (0.9524 $L{\cdot}mol^{-1}h^{-1}$ and 92.1 $kJ{\cdot}mol^{-1}$). Full-process simulation calculations with purities of all separated materials exceeding 99.5 % were obtained, indicating the rationality of the synthesis process. LCA analysis reveals that this reaction system exerts a comparatively low pressure on global environmental reference systems. Finally, the economic analysis revealed profits were predominantly concentrated within the range of 622.22 to 2909.06 USD/t, suggesting that the project could attain relatively high economic returns under most conditions. This study not only advances the mechanistic understanding of carbon-catalyzed BV oxidation but also pioneers a cost-effective and scalable strategy for biodegradable polymer synthesis, aligning with the global push for green chemistry and circular economy principles.

CRediT authorship contribution statement

Jiangnan Huang: Writing – original draft, Resources, Investigation, Data curation. **Chaoxu Chai:** Methodology, Investigation, Data curation. **Hongjuan Wang:** Resources, Methodology. **Hao-Fan Wang:** Resources, Methodology, Investigation. **Shuang Li:** Resources, Project administration. **Hao Yu:** Resources, Methodology. **Yonghai Cao:**

Writing – review & editing, Validation, Supervision, Software, Resources.

Declaration of competing interest

The authors declare that they have no known competing financial interests or personal relationships that could have appeared to influence the work reported in this paper.

Acknowledgements

We would like to acknowledge the financial support from the National Natural Science Foundation of China (22272056) and Guangdong Basic and Applied Basic Research Foundation (2022A1515140108), the Research Fund Program of Guangdong Provincial Key Laboratory of Fuel Cell Technology (FC202305), and the start-up fund from Zhongkai College of Agricultural Engineering. The authors extend their sincere gratitude to Jiefeng Zhou from South China University of Technology for his exceptional contributions in completing the Aspen simulation and optimization segment of this work. Dr. Yuting Wang from Beijing University of Petroleum contributed to the life cycle assessment analysis.

Appendix A. Supplementary data

Supplementary data to this article can be found online at https://doi.org/10.1016/j.ces.2025.122666.

Data availability

Data will be made available on request.

References

Arista, A.E., Putra, G.M.D., Adiaksa, N.V., Jaya, D.E.C., Kusuma, H.S., 2024. Bibliometric analysis and visualization for revealing publication trends research mapping of solid acid catalyst for biodiesel and biofuel production based on VOSviewer. Sci. Talks 9, 100295.

Az-Zahra, K.D., Jaya, D.E.C., Mutiara, X., Kusuma, H.S., 2024. Exploring research publication trends on clove oil as an antibacterial using bibliometric analysis with VOSviewer based on Scopus database. Sci. Talks 11, 100376.

Baeyer, A., Villiger, V., 1899. Einwirkung des Caro'schen Reagens auf Ketone. Ber. Dtsch. Chem. Ges. 32 (3), 3625–3633.

Brink, G.J.t., Arends, I., Sheldon, R.A. The Baeyer-Villiger reaction: New developments toward greener procedures Chem. Rev. 104 9 2004 4105 4123.

Cai, Z., Liu, D., Huang, J., Feng, J., Wang, H., Yang, G., Peng, F., Cao, Y., Yu, H., 2022. Solvent-Free production of ε-Caprolactone from Oxidation of Cyclohexanone Catalyzed by Nitrogen-Doped Carbon Nanotubes. Ind. Eng. Chem. Res. 61 (5), 2037–2044.

Cai, Z., Yuan, M., Wang, H., Wang, H.-F., Li, S., Cao, Y., Yu, H., Peng, F., 2025. Elucidating the Influence of N Doping on production of ε-Caprolactone Catalyzed by Nanocarbon: a Kinetic Model from batch to Semibatch and Continuous-Flow Operations. Ind. Eng. Chem. Res. 64 (9), 4845–4857.

Cao, X., Wu, X., Liu, Y., Geng, H., Yu, S., Liu, S., 2022. Boron and nitrogen co-doped porous carbon nanospheres for oxidative dehydrogenation of ethane to ethylene. Carbon 197, 120–128.

Cao, Y., Li, B., Zhong, G., Li, Y., Wang, H., Yu, H., Peng, F., 2018. Catalytic wet air oxidation of phenol over carbon nanotubes: Synergistic effect of carboxyl groups and edge carbons. Carbon 133, 464–473.

Cao, Y., Yu, H., Peng, F., Wang, H., 2014. Selective Allylic Oxidation of Cyclohexene Catalyzed by Nitrogen-Doped Carbon Nanotubes. ACS Catal. 4, 1617–1625.

Cao, Y., Yu, H., Wang, H., Peng, F., 2017. Solvent effect on the allylic oxidation of cyclohexene catalyzed by nitrogen doped carbon nanotubes. Catal. Commun. 88, 99–103.

Cao, Y.H., Yu, H., Tan, J., Peng, F., Wang, H.J., Li, J., Zheng, W.X., Wong, N.B., 2013. Nitrogen-, phosphorous- and boron-doped carbon nanotubes as catalysts for the aerobic oxidation of cyclohexane. Carbon 57, 433–442.

Chen, S.-Y., Zhou, X.-T., Wang, J.-X., Luo, R.-C., Luo, Q.-J., Yu, L.-J., Ji, H.-B., 2017. Promoting the aerobic Baeyer-Villiger oxidation of ketones over carboxylic multi-walled carbon nanotubes. Mol. Catal. 438, 152–158.

Chi, Y., Zhu, M., Li, Y., Yu, H., Wang, H., Peng, F., 2016. The effect of surface oxygenated groups of carbon nanotubes on liquid phase catalytic oxidation of cumene. Catal. Sci. Tech. 6 (7), 2396–2402.

Corma, A., Nemeth, L.T., Renz, M., Valencia, S., 2001. Sn-zeolite beta as a heterogeneous chemoselective catalyst for Baeyer–Villiger oxidations. Nature 412 (6845), 423–425.

Das, S., Chakravorty, A., Raj, A., Luktuke, S., Appu Mini, A., Awasthi, S., Sankar Sana, S., Kumar Pandey, S., Raghavan, V., 2024. Graphene/MWCNT/copper-nanoparticle fabricated printed electrode for diclofenac detection in milk and drinking water: Electrochemical and in-silico analysis. J. Mol. Liq. 411, 125750.

Estes, C.S., Gerard, A.Y., Godward, J.D., Hayes, S.B., Liles, S.H., Shelton, J.L., Stewart, T. S., Webster, R.I., Webster, H.F., 2019. Preparation of highly functionalized carbon nanoparticles using a one-step acid dehydration of glycerol. Carbon 142, 547–557.

Fu, H., Huang, K., Yang, G., Cao, Y., Wang, H., Peng, F., Wang, Q., Yu, H., 2020. Synergistic effect of Nitrogen Dopants on Carbon Nanotubes on the Catalytic Selective Epoxidation of Styrene. ACS Catal. 10 (1), 129–137.

Grammenos, A.O., André, R.F., Igoa Saldaña, F., Kamra, M., Antonietti, M., Odziomek, M., 2025. Harnessing the Electrochemical Hydrogen Storage Capability of N-Doped Carbons for Metal-Free Hydrogenations. ACS Catal. 4519–4532.

Hajivand, P., Carolus Jansen, J., Pardo, E., Armentano, D., Mastropietro, T.F., Azadmehr, A., 2024. Application of metal-organic frameworks for sensing of VOCs and other volatile biomarkers. Coord. Chem. Rev. 501, 215558.

Huang, J., Bai, J., Feng, J., Jiang, Q., Yang, G., Wang, H., Yu, H., Zhang, Q., Cao, Y., Peng, F., 2022. Catalytic Synthesis of Lactones from Alkanes in the Presence of Aldehydes and Carbon Nanotubes. ACS Sustain. Chem. Eng. 10 (20), 6713–6723.

Kusuma, H.S., Al Lantip, G.I., Mutiara, X., Arista, A.E., Az Zahra, K.D., Darmokoesoemo, H., Amenaghawon, A.N., 2024a. Bibliometric analysis of Rhodamine B degradation using cellulose-based materials: a review. Hybrid Adv. 5, 100159.

Kusuma, H.S., Az-Zahra, K.D., Saputri, R.W., Utomo, M.D.P., Jaya, D.E.C., Amenaghawon, A.N., Darmokoesoemo, H., 2024b. Unlocking the potential of agricultural waste as biochar for sustainable biodiesel production: a comprehensive review. Bioresour. Technol. Rep. 26, 101848.

Kusuma, H.S., Nida, R.A., Listiawati, V., Rahayu, D.E., Febryola, L.A., Darmokoesoemo, H., Amenaghawon, A.N., 2024c. Trends on adsorption of lead (Pb) using water hyacinth: Bibliometric evaluation of Scopus database. Environ. Res. 244, 117917.

Li, Y., Guo, M., Yin, S., Chen, L., Zhou, Y., Qiu, R., Au, C., 2013. Graphite as a highly efficient and stable catalyst for the production of lactones. Carbon 55, 269–275.

Liu, W., Wang, C., Herold, F., Etzold, B.J.M., Su, D., Qi, W., 2019. Oxidative dehydrogenation on nanocarbon: effect of heteroatom doping. Appl. Catal. b: Env 258, 117982.

Meng, Q., Hou, M., Liu, H., Song, J., Han, B., 2017. Synthesis of ketones from biomass-derived feedstock. Nat. Commun. 8, 14190.

Nabae, Y., Rokubuichi, H., Mikuni, M., Kuang, Y., Hayakawa, T., Kakimoto, M.-A., 2013. Catalysis by Carbon Materials for the Aerobic Baeyer–Villiger Oxidation in the Presence of Aldehydes. ACS Catal. 3 (2), 230–236.

Neuenschwander, U., Turra, N., Aellig, C., Mania, P., Hermans, I., 2010. Understanding Selective Oxidations. Chimia 64 (4), 225–230.

Pamin, K., Prończuk, M., Basąg, S., Kubiak, W., Sojka, Z., Połtowicz, J., 2015. A new hybrid porphyrin-heteropolyacid material: Synthesis, characterization and investigation as catalyst in Baeyer–Villiger oxidation. Synergistic Effect. Inorg. Chem. Commun. 59, 13–16.

Putra, N.R., Rizkiyah, D.N., Che Yunus, M.A., Kusuma, H.S., Darmokoesoemo, H., 2024. Mapping the landscape of clove oil as essential oil for health and wellness: a bibliometric review of advances, challenges, and future directions. J. Essent. Oil Bear Pl. 27 (2), 300–326.

Reichardt, C., Welton, T., 2011. Solvents and solvent effects in organic chemistry. John Wiley & Sons, Weinheim.

Sharma, A., Mudahar, I., Sharma, H., 2022. Carbon nanotubes with periodic vacancy defects to phenine nanotubes: a DFT study. Comput. Theor. Chem. 1211, 113692.

Singh, N., Ogunseitan, O.A., Wong, M.H., Tang, Y., 2022. Sustainable materials alternative to petrochemical plastics pollution: a review analysis. Sustainable Horiz. 2, 100016.

Stolze, K., Udilova, N., Nohl, H., 2002. ESR analysis of spin adducts of alkoxyl and lipid-derived radicals with the spin trap Trazon. Biochem. Pharmacol. 63 (8), 1465–1470.

Su, D.S., Perathoner, S., Centi, G., 2013. Nanocarbons for the development of advanced catalysts. Chem. Rev. 113 (8), 5782–5816.

Su, D.S., Wen, G., Wu, S., Peng, F., Schlogl, R., 2017. Carbocatalysis in Liquid-phase Reactions. Angew. Chem. Int. Ed. 56 (4), 936–964.

Su, Y., Huang, J., Yang, G., Wang, H., Yu, H., Zhang, Q., Cao, Y., Peng, F., 2023. Elucidating mechanism of ethylbenzene oxidation catalyzed by carbon-based catalysts with kinetic modeling. AIChE J 69 (5), e18007.

Sun, G., Cao, X., Wang, Y., Sun, X., Chen, Q., 2024. Comparative life cycle assessment of two different waste materials for recycled fiber. Resour. Conserv, Recycl, p. 205.

Tang, P., Hu, G., Li, M., Ma, D., 2016. Graphene-based Metal-Free Catalysts for Catalytic Reactions in the liquid phase. ACS Catal. 6 (10), 6948–6958.

Timokhin, V.I., Lisovska, M.T., Pokutsa, A.P., 2000. Kinetics and mechanism of cyclohexane oxidation with molecular oxygen in the presence of propionic aldehyde. Kinet. Catal. 41 (2), 159–165.

Ueda, J.-I., Saito, N., Ozawa, T., 1996. Detection of Free Radicals Produced from Reactions of Lipid Hydroperoxide Model Compounds with Cu(II) Complexes by ESR Spectroscopy. Arch. Biochem. Biophys. 325 (1), 65–76.

Wang, J., Chen, X., Sim, L.B., Guan, L., He, X., Zhou, X., Chen, B., 2024. Unraveling the mechanism and kinetics of aerobic Baeyer Villiger oxidation of cyclohexanone. AIChE J 70 (1), e18263.

Wei, S., Chen, Y., Qiu, Y., Kong, W., Lin, D., Li, J., Lan, G., Jia, Y., Sun, X., Cheng, Z., Liu, J., Hu, P., Li, Y., 2025a. The curvature structure unlocks an ultra-efficient metal-free carbon catalyst surpassing gold for acetylene hydrochlorination. Chin. J. Catal. 70, 260–271.

Wei, S., Lan, G., Qiu, Y., Lin, D., Kong, W., Li, Y., 2025b. Advances in metal-free carbon catalysts for acetylene hydrochlorination: from heteroatom doping to intrinsic defects over the past decade. Chin. J. Catal. 70, 8–43.

Woodruff, M.A., Hutmacher, D.W., 2010. The return of a forgotten polymer—Polycaprolactone in the 21st century. Prog. Polym. Sci. 35 (10), 1217–1256.
Yang, W.-C., Feng, J.-G., Wu, L., Zhang, Y.-Q., 2019. Aliphatic Aldehydes: Novel Radical Alkylating Reagents. Adv. Synth. Catal. 361 (8), 1700–1709.
Yang, X., Cao, Y., Yu, H., Huang, H., Wang, H., Peng, F., 2017. Unravelling the Radicals transition during the Carbon-catalyzed Oxidation of Cyclohexane by In-Situ Electron Paramagnetic Resonance in liquid phase. Catal. Sci. Tech. 7 (19), 4431–4436.
Yang, X., Wang, H., Li, J., Zheng, W., Xiang, R., Tang, Z., Yu, H., Peng, F., 2013. Mechanistic insight into catalytic oxidation of cyclohexane over carbon nanotubes: kinetics and in-situ spectroscopic evidences. Chem Eur J 19 (30), 9818–9824.
Yang, Y., Du, W., Qian, G., Duan, X., Gu, X., Zhou, X., Yang, Z., Zhang, J., 2023. Kinetically guided high-yield and rapid production of ε-caprolactone in a microreactor system. AIChE J 69 (3), e17867.
Yu, H., Peng, F., Tan, J., Hu, X., Wang, H., Yang, J., Zheng, W., 2011. Selective Catalysis of the Aerobic Oxidation of Cyclohexane in the liquid phase by Carbon Nanotubes. Angew. Chem. Int. Ed. 50 (17), 3978–3982.
Zhang, X., Hu, A., Li, S., Feng, R., Huang, S., Xie, Z., 2024. N, P codoped hollow carbon prisms for efficient oxidative dehydrogenation reaction with both enhanced activity and selectivity. Chem. Eng. J. 486, 150249.
Zhao, B., Xu, J., Gao, D., Chen, F., Wang, X., Liu, T., Wu, X., Yu, H., 2024. Spatially separated HOMO-LUMO sites in highly intra- and inter-plane crystalline g-C3N4 photocatalyst for exceptional H2 generation. Appl. Catal. B Environ. Energy 355, 124215.
Zou, Y., Wang, X., Khan, A., Wang, P., Liu, Y., Alsaedi, A., Hayat, T., Wang, X., 2016. Environmental Remediation and Application of Nanoscale Zero-Valent Iron and its Composites for the Removal of Heavy Metal Ions: a Review. Environ. Sci. Technol. 50 (14), 7290–7304.